bioRxiv preprint doi: https://doi.org/10.1101/2023.05.10.540292; this version posted May 11, 2023. The copyright holder for this preprint (which was not certified by peer review) is the author/funder, who has granted bioRxiv a license to display the preprint in perpetuity. It is made available under aCC-BY-NC-ND 4.0 International license.

Spatial biology of Ising-like synthetic genetic networks

Kevin Simpson[1], Juan Keymer[2,3,4], Fernán Federici[1,5,6]

May 11, 2023

1. ANID - Millennium Science Initiative Program - Millennium Institute for Integrative Biology (iBio), Santiago, Chile.
2. IAS, X-Institute, Shenzhen, China.
3. Schools of Physics and Biology, Pontificia Universidad Católica de Chile, Santiago, Chile.
4. Department of Natural Sciences and Technology, Universidad de Aysén, Coyhaique, Chile.
5. Institute for Biological and Medical Engineering, Schools of Engineering, Medicine and Biological Sciences, Pontificia Universidad Católica de Chile, Santiago, Chile.
6. FONDAP Center for Genome Regulation. Department of Molecular Genetics and Microbiology, Pontificia Universidad Católica de Chile, Santiago, Chile.

* Corresponding Author: Juan Keymer juan.keymer@gmail.com, Fernán Federici ffederici@bio.puc.cl.

Keywords: Ising model, bi-stable, synthetic gene networks, spatial correlation, criticality

bioRxiv preprint doi: https://doi.org/10.1101/2023.05.10.540292; this version posted May 11, 2023. The copyright holder for this preprint (which was not certified by peer review) is the author/funder, who has granted bioRxiv a license to display the preprint in perpetuity. It is made available under aCC-BY-NC-ND 4.0 International license.

Abstract

Understanding how spatial patterns of gene expression emerge from the interaction of individual gene networks is a fundamental challenge in biology. Developing a synthetic experimental system with a common theoretical framework that captures the emergence of short- and long-range spatial correlations (and anti-correlations) from interacting gene networks could serve to uncover generic scaling properties of these ubiquitous phenomena. Here, we combine synthetic biology, statistical mechanics models and computational simulations to study the spatial behavior of synthetic gene networks (SGNs) in *Escherichia coli* colonies. Guided by the combined mechanisms of the contact process lattice simulation and two-dimensional Ising model (CPIM), we describe the spatial behavior of bi-stable and chemically-coupled SGNs that self-organize into patterns of long-range correlations with power-law scaling or short-range anti-correlations. These patterns, resembling ferromagnetic and anti-ferromagnetic configurations of the Ising model near critical points, maintain their scaling properties upon changes in growth rate and cell shape. This robust spatial behavior could provide insights into the study and engineering of self-organizing patterns of genetic networks in eukaryotic tissues and bacterial consortia.

bioRxiv preprint doi: https://doi.org/10.1101/2023.05.10.540292; this version posted May 11, 2023. The copyright holder for this preprint (which was not certified by peer review) is the author/funder, who has granted bioRxiv a license to display the preprint in perpetuity. It is made available under aCC-BY-NC-ND 4.0 International license.

Introduction

The emergence of spatially-correlated structures is a phenomenon that pervades biology from molecular to ecological scales (e.g. Noble *et al* (2018); Bray and Duke (2004); Duke *et al* (2001); Turing (1990)). An emblematic case of research is the spatial correlations of gene expression in eukaryotic tissues and microbial communities, which can occur at short-range or at the scale of the whole population (e.g.van Vliet *et al* (2018); Rosenthal *et al* (2018); Kim *et al* (2019); van Gestel *et al* (2021)). For instance, negative spatial correlations can emerge during eukaryotic cell differentiation (e.g.Collier *et al* (1996)) and metabolic cross-feeding in microbial systems (e.g.Dal Co *et al* (2020); Cole *et al* (2015); Lovley (2017)), whereas positive gene spatial correlations can be observed during the synchronization of growth and resource sharing in bacterial populations (e.g. Liu *et al* (2017, 2015); van Vliet *et al* (2022)). These spatial patterns are shaped from the bottom-up through mechanisms that differ widely across different organisms. Developing a common experimental system and theoretical framework that capture the formation of short- and long-range spatial correlations (and anti-correlations) from interacting gene networks could serve to uncover generic mechanisms and scaling properties of these ubiquitous phenomena. The required theoretical framework should embody the emergence of global correlations from the collective behaviour of interacting gene networks in space. The Ising model from statistical mechanics is suitable for this task since it provides a mathematical machinery, amenable to simple numerical simulations and exact analysis, able to address the collective behaviour of spatially-interacting particles. Originally formulated to understand the loss of magnetism in ferromagnetic materials as the temperature increases, this model has been useful to study second order phase transitions and critical phenomena (Ising (1925); Kobe (1997); Solé (2011)). Different studies have demonstrated the applicability of the Ising model to investigate the spatial organization of biological processes at molecular, cellular and ecological scales. It has been used to explain the propagation of allosteric states in large multi-protein complexes (Bray and Duke (2004); Duke *et al* (2001)) as well as the emergence of long-range synchronization in ecological systems (Noble *et al* (2015, 2018)). At a cellular level, the Ising model has been used to study follicle alignment during mammalian hair patterning (Wang *et al* (2006)), ferromagnetic and anti-ferromagnetic correlations in lattices of hydrodynamically coupled bacterial vortices (Wioland *et al* (2016)), and continuous phase transitions in simulations of bacterial cell ensembles carrying coupled toggle switches (Weber and Buceta (2016)). Interestingly, the numerical simulations of (Weber and Buceta (2016)) suggest that gene regulatory networks constructed of toggle switches interconnected with quorum sensing signals exhibit spontaneous symmetry breaking, shedding light into the use of a minimal framework based on critical phenomena for phase transitions in cell groups. Applying the Ising model to the study of gene spatial correlations in natural cell populations could be challenging since these systems are embedded in complex physiological contexts affected by unknown components and unforeseen interactions. Alternatively, this phenomenon could be studied in synthetic gene networks (SGNs) that embody the essential features of the Ising model. The use of SGNs as test-beds to challenge biological theory has gained popularity since it provides more experimental control and analytical power (Gardner *et al* (2000); Elowitz and Leibler (2000); Mukherji and van Oudenaarden (2009); Elowitz and Lim (2010); Davies (2017)). The use of efficient DNA fabrication methods, well-characterized components and mathematical modeling has enabled the engineering SGNs of unprecedented scale and predictability (e.g. (Nielsen *et al* (2016)). This approach has enabled the engineering of biological patterns, a new frontier of interdisciplinary research that employ minimal and reconfigurable SGNs (Luo *et al* (2019); Schaerli *et al* (2014); Basu *et al* (2005); Payne *et al* (2013); Toda *et al* (2018); Ebrahimkhani and Ebisuya (2019)). The use of controllable SGNs embodying Ising model rules could be instrumental for defining a common theoretical ground for the spatial biology of gene networks.

Here, we apply a theoretical framework based on the Ising model to study how spatial correlations emerge from chemically-coupled, bi-stable SGNs in *Escherichia coli*. By analogy with the two-state interacting particles of the model, we construct synthetic toggle switches (Gardner *et al* (2000)) whose states are chemically-coupled by quorum sensing signalling (Grant *et al* (2016)). These SGNs self-organize in long-range spatial correlations and fractal patterns reminiscent of ferromagnetic systems of the Ising model. Inverting the response to the coupling signals, on the other hand, creates negative correlations similar to anti-ferromagnetic configurations, demonstrating correspondence between SGNs and the model.

bioRxiv preprint doi: https://doi.org/10.1101/2023.05.10.540292; this version posted May 11, 2023. The copyright holder for this preprint (which was not certified by peer review) is the author/funder, who has granted bioRxiv a license to display the preprint in perpetuity. It is made available under aCC-BY-NC-ND 4.0 International license.

Results

A two-dimensional Ising model in growing cell populations

To study how long-range gene correlations arise from diffusion-limited chemical coupling between gene networks, we employed the Ising model with two-state particles arranged on a two-dimensional lattice (Fig. 1a). To implement it in a growing population of cells, we generated a lattice model that combines the Contact Process (Harris (1974)), representing cell population dynamics, with the two-dimensional Ising model using the Metropolis algorithm (Metropolis *et al* (1953)). This model, hereafter named CPIM (for "Contact Process Ising Model"), consists of an interacting particle system that follows colonization, extinction and differentiation dynamics of particles on a two-dimensional lattice $\mathcal{L}$ of N sites (Fig. 1b). As in the Ising model, cells are fixed in their position and can only interact with its nearest four neighbours with an interaction energy $\mathcal{H}$, which in the absence of external perturbations is determined by the Hamiltonian:

$$\mathcal{H} = -J \sum_{\langle ij \rangle}^{N} \sigma_i \sigma_j \tag{1}$$

where σ corresponds to the state of differentiated cells (red or green, $+1$ or -1), $\langle ij \rangle$ indicates that the sum is only between neighbouring pairs of cells (only short-range interactions are allowed), and J represents the contribution to free energy made by the coupling interaction between these pairs of cells. We assumed that $J = +1$ for ferromagnetic systems and $J = -1$ for anti-ferromagnetic systems. This implies that the interaction energy between neighbouring cells is minimized when they have the same state in a ferromagnetic system, or the opposite state in an anti-ferromagnetic system (Eq. 1). In the Ising model, the probability P (in equilibrium) of a certain spatial configuration of spins x is defined by $P(H_x) = \frac{1}{Z} e^{-H_x/k_B T}$, where k_B is the Boltzmann constant, Z is the partition function $Z = \sum e^{-H_i/k_B T}$ (sum over all possible configurations), and T is the absolute temperature of the system. Together with Eq. 1, these equations show the contribution of J and T to the probability distribution of spatial configurations: for a given value of J, varying T determines the transition between ordered and disordered configurations of the system (Fig. 1a). Since we are interested in studying the emergence of gene correlations due to coupling between gene networks, in CPIM, T represents a parameter that regulates coupling in the system: a small value of T allows for a strong coupling, while a large value represents a weak coupling.

The net magnetization of a population (M), which represents the order parameter of the system, is determined by the degree of alignment of the cells, and is given by $M = \sum_i s_i$. The mean magnetization pero site ($|M/N|$) calculated for ferromagnetic populations simulated with CPIM (Fig. S1a) showed good agreement with the behaviour observed in the Ising model (Ibarra-García-Padilla *et al* (2016)). Fig. 1c shows the different cellular state configurations that emerge in simulated populations depending on the strength of the coupling (the value of T) and the type of interaction (ferromagnetic or anti-ferromagnetic). In a ferromagnetic population (Fig. 1c top), a strong interaction between cells ($T < T_c$) favours the alignment of states, leading to the emergence of large homogeneous patches of the same state. A further increase in the coupling ($T << T_c$) leads to colonies with cells in only one state. On the other hand, when the coupling between cells is weak ($T > T_c$), cells freely change their states regardless the state of their neighbours, leading to a colony with a noise-like appearance. Near a critical value of coupling ($T = T_c$), colonies spontaneously self-organize into patterns that resemble the long-range correlations and power-law decaying fractal objects described by universality class exponents of the Ising model at phase transition. At this critical point, the autocorrelation function of the simulated populations follows a power-law decay given by $C(r) = A\frac{exp(-r/B))}{r^{\eta}}$ (Fig. S1b), with a critical exponent of the autocorrelation function $\eta = 0.2518$, consistent with the value reported for the Ising model at the critical temperature ($\eta = 0.250$) (Ibarra-García-Padilla *et al* (2016)). This behavior close to the critical transition is particularly relevant since it links the short-range coupling between cellular states to the generation of macroscopic long-range correlations.

In anti-ferromagnetic populations, an ordered configuration emerges under strong interactions between cells and a disordered configuration is observed when the interaction is weak (Fig. 1c bottom). However, opposite states between neighbouring cells are favoured in the ordered configuration, resulting in the emergence of a checkerboard-like pattern of cellular states (a red cell surrounded by four green cells and vice versa). Near the critical value, colonies are composed of patches of checkerboard-like patterns separated by

bioRxiv preprint doi: https://doi.org/10.1101/2023.05.10.540292; this version posted May 11, 2023. The copyright holder for this preprint (which was not certified by peer review) is the author/funder, who has granted bioRxiv a license to display the preprint in perpetuity. It is made available under aCC-BY-NC-ND 4.0 International license.

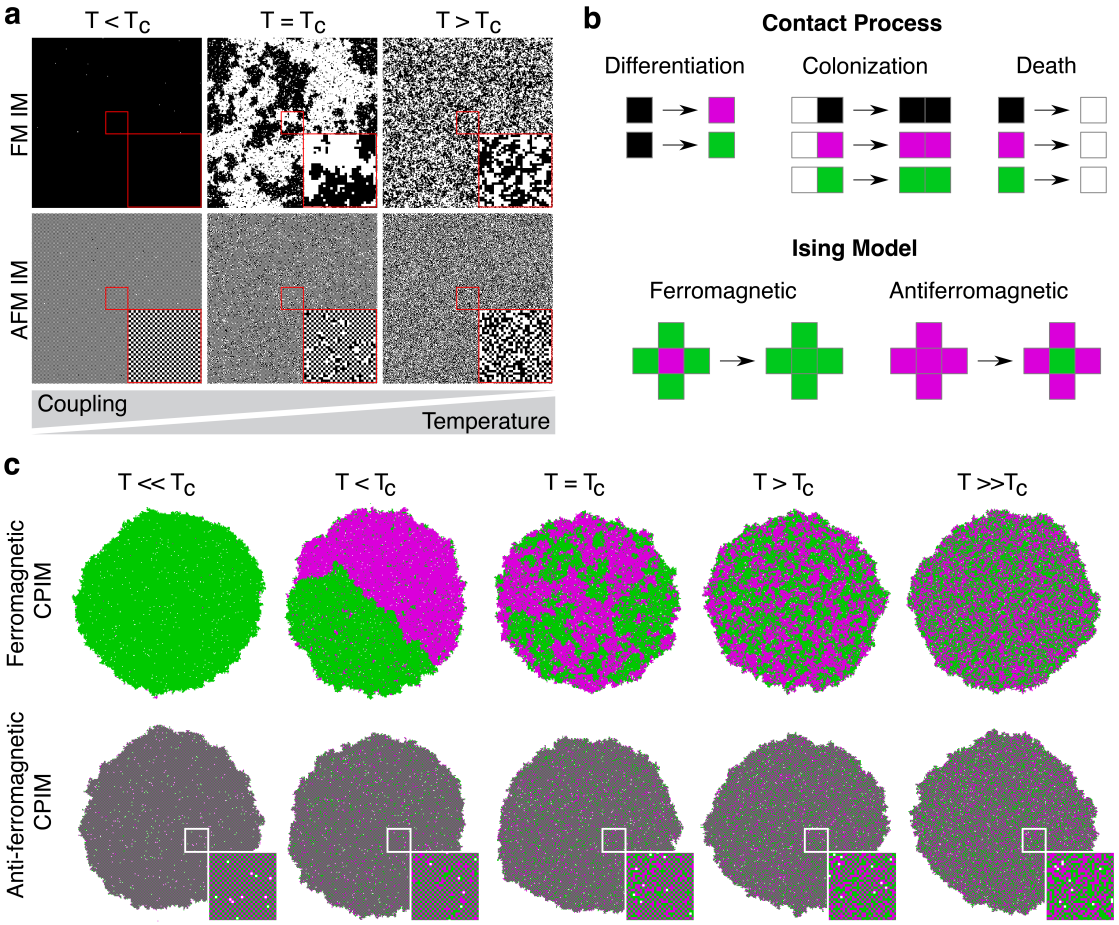

Figure 1: **Ising-like interactions in a growing population of cells.** (a) Numerical simulations of the two-dimensional ferromagnetic (FM IM) and anti-ferromagnetic (AFM IM) Ising model on a 250x250 lattice at different temperatures T relative to the critical temperature T_c. White and black squares represent the spin orientations $\sigma = \pm 1$. Insets correspond to a magnification of a 30x30 square in the center of the images. (b) Basic rules that define CPIM simulations. Top: Contact process lattice reactions of colonization, differentiation and death processes; bottom, Ising-like cellular state change mechanisms. Each site of this lattice can be in one of four states $S = \{\varnothing, *, +1, -1\}$, which represent vacant locations ($\varnothing$, white squares), locations occupied by undifferentiated cells ($*$, black squares), and locations occupied by differentiated cells in red ($+1$, magenta squares) or green (-1, green squares) state. (c) CPIM numerical simulations of growing ferromagnetic and anti-ferromagnetic cell populations at different values of the control parameter T relative to the critical value T_c. In the CPIM simulations, T represents a parameter that determines the strength of coupling between cells. Insets show a magnification of the square in the center of anti-ferromagnetic colonies showing a detail of the checkerboard-like pattern.

bioRxiv preprint doi: https://doi.org/10.1101/2023.05.10.540292; this version posted May 11, 2023. The copyright holder for this preprint (which was not certified by peer review) is the author/funder, who has granted bioRxiv a license to display the preprint in perpetuity. It is made available under aCC-BY-NC-ND 4.0 International license.

disordered regions.

These CPIM simulations showed that growing cell populations with ferromagnetic and antiferromagnetic Ising-like interactions give rise to short and long-range correlations around critical points. This suggests that SGNs with two states coupled through chemical signals that capture ferromagnetic and antiferromagnetic interactions should lead to spatial patterns of positive or negative correlations, respectively.

Synthetic gene networks with spin-like behaviour

We constructed synthetic gene circuits capturing Ising mechanisms, i.e. two states and coupling interactions (Fig. 2). We named these systems ferromagnetic or anti-ferromagnetic depending on whether they promote the same or opposite state in their neighbours, respectively (Fig. 2a). Each system is composed of three main functions: *i*) a state reporter, responsible for the synthesis of a red fluorescent protein (mCherry2, hereafter called "RFP" for simplicity) or a green fluorescent protein (sfGFP, hereafter called "GFP" for simplicity) to report the state of SGNs, *ii*) a switch module, composed of two repressors (LacI and TetR) that repress the expression of each other, allowing cells to adopt only one of the two possible states at a time, and *iii*) a coupling module, which allows the production of one of the two coupling signals for each state (3-oxo-C6-homoserine lactone (C6HSL), synthesised by LuxI from *Vibrio fischeri*, or 3-oxo-C12-homoserine lactone (C12HSL), synthesised by LasI from *Pseudomonas aeruginosa*). These functions are contained in two vectors: the reporter vector and the ferromagnetic or anti-ferromagnetic vector (Fig. 2b). The expression of genes encoding the repressors, red/green fluorescent protein, and C6HSL and C12HSL biosynthetic enzymes are under the control of two inducible/repressible promoters: the pLuxpTet promoter (induced by C6HSL and repressed by TetR) and the pLaspLac promoter (induced by C12HSL and repressed by LacI). To gain orthogonality, we used the pLux76 and pLas81 version of the pLux and pLas promoters, respectively (Grant *et al* (2016)) (hereafter named pLux76pTet and pLas81pLac). Thus, the states of these SGNs are determined by the coupling molecules and their ferromagnetic or anti-ferromagnetic configurations. In the ferromagnetic vector, cells synthesize the same coupling molecule they sense, inducing the same state in neighbouring cells. Conversely, in the anti-ferromagnetic vector, cells synthesize the opposite coupling signal they sense, inducing the opposite state in neighboring cells. In both systems, the *LacI* and *TetR* repressors are under the pLux76pTet and pLas81pLac promoters, respectively, ensuring that the production of one coupling signal is accompanied by the repression of the other.

To test the bi-stability condition and coupling properties of the ferromagnetic and anti-ferromagnetic systems, we calculated the red and green fluorescent protein synthesis rate (Rudge *et al* (2016)) in *E. coli* cells grown in different concentrations of the coupling signals C6HSL and C12HSL (Fig. 2c-f and S2). To model SGNs behaviour, we considered a simplified version in which each dual promoter (pLux76pTet and pLas81pLac) have two states: an active state that allows the expression of the fluorescent protein gene (ON state), and an inactive state with no expression of this gene (OFF state) (Keymer *et al* (2006)). The probability P of finding each promoter in the active state at equilibrium is:

$$P_{on} = \left(1 + \left[\frac{1 + [L]/K_d^{off}}{1 + [L]/K_d^{on}}\right]^n \cdot e^{-n\beta\Delta E}\right)^{-1} \tag{2}$$

where L is the concentrations of the coupling signal (the ligand), $\Delta E = E_{off} - E_{on}$ represents the energy difference between inactive and active promoter without ligand bound, K_d^{on} and K_d^{off} are the dissociation constants that characterize the binding of ligands to active and inactive promoters, respectively; and n is a Hill exponent to represents cooperative binding (Keymer *et al* (2006)).

In a population of cells carrying only the reporter vector, the probability of finding *RFP* and *GFP* promoters active in absence of the inducers C6HSL and C12HSL is close to zero, and it increases as the concentration of its inducer increases (Fig. S2). This behaviour is reflected in the negative values of ΔE and that $K_d^{on} << K_d^{off}$ (Table S2). At very low concentrations of inducers, a population of ferromagnetic cells is only in the green state (Fig. 2c, d). This means that the probability of finding the *GFP* promoter active is 1 ($\Delta E > 0$), while the probability of finding the *RFP* promoter active is 0 ($\Delta E < 0$) (Table S3), suggesting that the system is biased towards the production of C12HSL. Accordingly, the pLas promoter has been shown to have a higher basal expression than the pLux promoter (Kylilis *et al* (2018); Grant *et al* (2016)). Since in this system the pLas81pLac promoter directs the expression of *LasI*, its higher basal expression drives cells

bioRxiv preprint doi: https://doi.org/10.1101/2023.05.10.540292; this version posted May 11, 2023. The copyright holder for this preprint (which was not certified by peer review) is the author/funder, who has granted bioRxiv a license to display the preprint in perpetuity. It is made available under aCC-BY-NC-ND 4.0 International license.

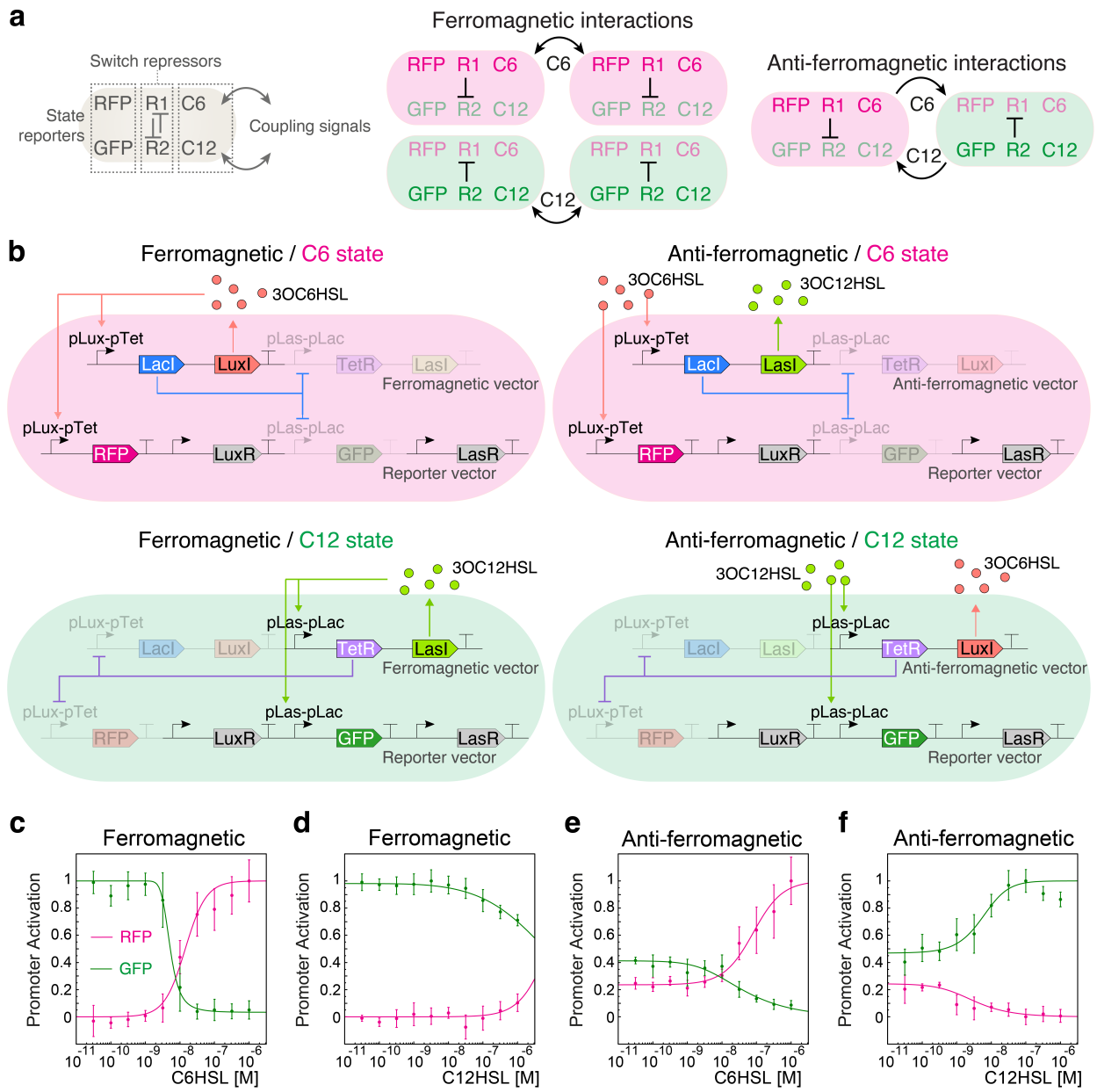

Figure 2: **Ferromagnetic and anti-ferromagnetic configurations of coupled, bi-stable synthetic gene networks.** (a) Schematic representation of ferromagnetic and anti-ferromagnetic interactions between two neighbouring cells. The states, defined by the expression of a red (mCherry2 labelled as "RFP" for simplicity) or green (sfGFP, labelled as "GFP" for simplicity) fluorescent proteins, are determined by mutually inhibiting repressors R1 and R2. Cell states are coupled, in ferromagnetic and anti-ferromagnetic configurations, with neighbouring cells by diffusive signals C6 and C12. (b) Gene network arrangement of ferromagnetic and anti-ferromagnetic systems in C6 and C12 states. Ferromagnetic and anti-ferromagnetic systems are composed of a ferromagnetic or anti-ferromagnetic vector and a reporter vector. LasR-C12 and LuxR-C6 complexes were omitted for simplicity. (c-f) Red and green fluorescent protein synthesis rate of *E. coli* cells carrying ferromagnetic (c,d) and anti-ferromagnetic (e,f) systems, grown in liquid medium supplemented with different concentrations of C6HSL (left) and C12HSL (right). Points and error bars correspond to the mean of the fluorescent protein synthesis rates normalized by its maximum value reached in each system and the standard deviation of 4 biological replicates, while lines correspond to the fitting of Eq. 2.

bioRxiv preprint doi: https://doi.org/10.1101/2023.05.10.540292; this version posted May 11, 2023. The copyright holder for this preprint (which was not certified by peer review) is the author/funder, who has granted bioRxiv a license to display the preprint in perpetuity. It is made available under aCC-BY-NC-ND 4.0 International license.

to produce basal amounts of C12HSL, generating a population of cells in the same state. This also explains why the external addition of C12HSL did not induce a major change in the synthesis rates of fluorescent proteins, except at very high concentrations of this inducer (Fig. 2d) at which signal crosstalk starts to play a relevant role in the activity of the promoters (Grant *et al* (2016)). At around 10^{-8} M of C6HSL, there is a drastic decrease in the probability of finding the *GFP* promoter active, which is accompanied by an increase in the probability of finding the *RFP* promoter active (Fig. 2c) (compare the values of K_d^{on} and K_d^{off} for each promoter in Table S3). Thus, depending on the concentration of C6HSL in the medium, a population of cells carrying the ferromagnetic system can be in one of 3 states: all cells in the green state (low C6HSL), all cells in the red state (high C6HSL), or a mix of red and green cells (around 10^{-8} M of C6HSL). These results suggest that a population of ferromagnetic cells can change between red and green states depending on the concentration of C6HSL in the medium.

In a population of cells carrying the anti-ferromagnetic system, the probability of finding the *GFP* and *RFP* promoters active is different from zero at very low concentrations of inducers (Fig. 2e, f), with values of ΔE closer to 0 (Table S4). In this condition, a population of anti-ferromagnetic cells is in a mixed state, with red and green cells. Microscope analysis of cells in the mixed state revealed that there is no "yellow" cells (data not shown), indicating that individual cells can only be in red or green state at a time. Since *LuxI* is under the control of the pLas81pLac promoter, cells produce a basal amount of C6HSL. Contrary to the case of the ferromagnetic system, this induces the opposite state in other cells, inducing them to produce C12HSL and leading to a balance in the production of both coupling signals. Increasing the concentration of C6HSL in the medium induces an increase in the probability of finding the *RFP* promoter active and a decrease in the probability of finding the *GFP* promoter active (Fig. 2e), while increasing the concentration of C12HSL produces the opposite effect (Fig. 2f). These results show that a population of anti-ferromagnetic cells can change from a mixed state to a population in a red or green state depending on the concentration of the coupling signals in the medium.

These results suggest that both ferromagnetic and anti-ferromagnetic systems are able to couple states in liquid culture, a required property for the emergence of Ising-like pattern when cells are spatially distributed (i.e. grown in solid media) (Fig. 1).

Ising-like patterns in ferromagnetic and anti-ferromagnetic populations

To test whether the SGNs were able to achieve Ising-like patterns of gene expression such as those observed in CPIM simulations, we studied the fluorescent patterns that emerge in colonies of *E. coli* cells carrying the reporter and ferromagnetic or anti-ferromagnetic vectors. In order to discard any bias related to the properties of the reporters, we constructed another version of the reporter vector in which the promoters directing the expression of the red and green fluorescent proteins are swapped (Fig. S3). To counteract the higher basal expression of the promoter induced by C12HSL and make red and green states equally likely, ferromagnetic and anti-ferromagnetic cells were grown on solid medium supplemented with different concentrations of C6HSL (Fig. S4). As observed in liquid cultures, ferromagnetic colonies were found to be only in one state in absence (or at very low concentrations) of C6HSL: green for the reporter vector 1 and red for the reporter vector 2 (Fig. S4a). However, growing ferromagnetic cells on solid medium with 10^{-8} M of C6HSL led to the generation of spatial patterns of red and green cellular state domains across the colonies (Fig. S4 a and S5), in accordance with the state transition found in liquid cultures (Fig. 2c). A high concentration of C6HSL (10^{-7} M) also produced colonies in only one state but opposite to that of colonies grown at low concentrations of the inducer (Fig. S4a). At this point, global exogenous concentration of C6HSL appeared to dominate the system over the cell-cell coupling between networks.

Anti-ferromagnetic colonies showed a spatial pattern of red and green domains in the absence (and at very low concentrations) of C6HSL (Fig. S4b). Under this condition, the center of colonies was dominated by cells in green (reporter vector 1) or red state (reporter vector 2), while the periphery was mainly composed of cells in the opposite state. Due to the higher basal expression of the pLas81pLac promoter, all anti-ferromagnetic cells that give rise to colonies are mostly in the same state. Although these cells synthesize basal amounts of C6HSL, it is not enough to counteract the effects of the basal expression of the promoter in neighbouring cells to induce the opposite state, generating a sector of the colony dominated by cells in one state. At some point during the growth of the colony, the C6HSL accumulated in the medium allows cells to change states regardless of promoter basal expression, generating a sector with a mix of red and green domains. As cells

bioRxiv preprint doi: https://doi.org/10.1101/2023.05.10.540292; this version posted May 11, 2023. The copyright holder for this preprint (which was not certified by peer review) is the author/funder, who has granted bioRxiv a license to display the preprint in perpetuity. It is made available under aCC-BY-NC-ND 4.0 International license.

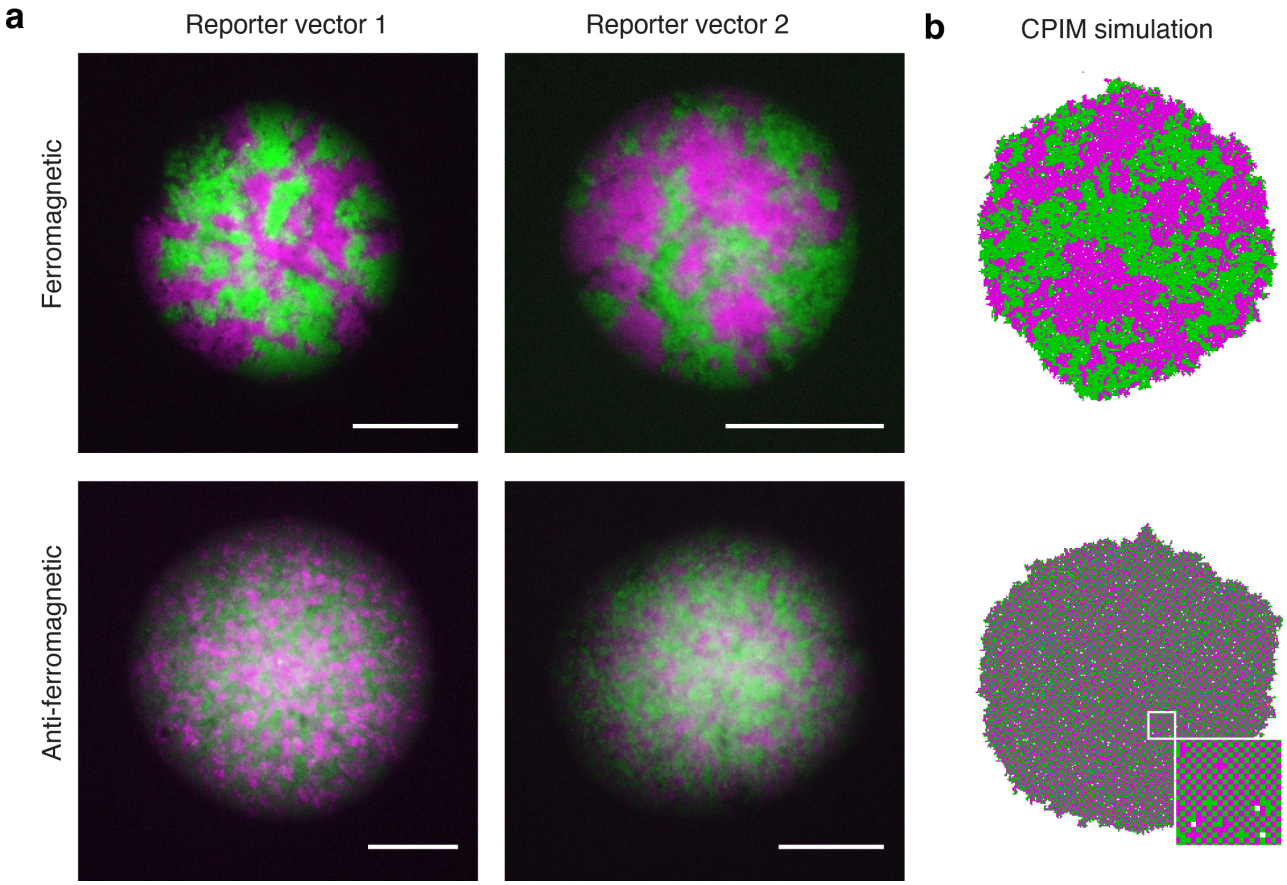

Figure 3: **Self-organized patterns of cellular states in ferromagnetic and anti-ferromagnetic colonies.** a) Representative images of red and green fluorescent protein patterns that emerge in colonies of spherical *E. coli* cells carrying the ferromagnetic or anti-ferromagnetic systems with reporter vector 1 or 2. Cells were grown on solid M9-glucose medium supplemented with 10^{-8} M of C6HSL, a concentration that counteracts the bias introduced by the basal expression of the pLas81pLac promoter. Images were taken approximately 18 hours after inoculation. Scale bars 100 μm. Red cells are shown in magenta. b) Images obtained from populations simulated with CPIM are included for comparison.

bioRxiv preprint doi: https://doi.org/10.1101/2023.05.10.540292; this version posted May 11, 2023. The copyright holder for this preprint (which was not certified by peer review) is the author/funder, who has granted bioRxiv a license to display the preprint in perpetuity. It is made available under aCC-BY-NC-ND 4.0 International license.

continue synthesizing C6HSL, it accumulates to a concentration that triggers a ring of the opposite state in newly born cells in the periphery of the colony. As in ferromagnetic colonies, red and green cellular state domains emerged across the whole colony at 10^{-8} M of C6HSL (Fig. S4b and S5). Compared to those patterns in ferromagnetic colonies at the same C6HSL concentration, the red and green domains generated in anti-ferromagnetic colonies are much smaller. A further increase in the concentration of C6HSL in the medium (10^{-7} M) only produced colonies in the red (reporter vector 1) or green (reporter vector 2) state (Fig. S4b).

These results show that ferromagnetic and anti-ferromagnetic SGNs allow the self-organization of distinctive patterns in *E. coli* colonies, as partially anticipated by the CPIM simulations (Fig. 1c). However, the formation of fractal-like jagged patterns, characteristic of rod-shaped non-motile *E. coli* cells, caused these patterns to visually differ from those obtained with simulations. These fractal patterns are the result of both mechanisms at play: the chemical coupling and the buckling instabilities generated by the polar cell shape that propagate due to the uni-axial cell growth and division (Rudge *et al* (2013)).

In order to analyze the pattern generated by the ferromagnetic and anti-ferromagnetic systems without the influence of uniaxial cell growth, we used the *E. coli* mutant strain KJB24 that forms spherical cells. This strain performs cell division in any direction due to a mutation in *RodA* (Begg and Donachie (1998)), removing the cell polarity-driven buckling instabilities that give rise to jagged patterns (Rudge *et al* (2013)). As observed in colonies of rod-shaped cells, C6HSL increases only the red or green fluorescence of colonies of spherical cells carrying only the reporter vector 1 or 2 (Fig. S6), respectively. In accordance with the findings on colonies of rod-shaped cells, ferromagnetic Ising-like patterns emerged in colonies of ferromagnetic spherical cells when they were grown in the range of 10^{-8} M of C6HSL, regardless of the reporter vector used (Fig. 3). These patterns look qualitatively more similar to those observed in CPIM simulated ferromagnetic populations than the patterns generated by rod-shaped ferromagnetic cells. Anti-ferromagnetic colonies of spherical cells showed a characteristic pattern of small domains of red and green states at 10^{-8} M of C6HSL (Fig. 3).

To compare the patterns that emerged in colonies to those observed in simulated populations, we calculated the Hamming distance (Fig. S7) between colonies of ferromagnetic spherical cells and simulated ferromagnetic populations around the critical value of T ($T_c = 2.27$) (Fig. S7a, magenta dots). The Hamming distance between two images of equal size is the number of pixel positions at which the value of those pixels are different. Therefore, the smaller the Hamming distance between two images, the more similar those images are. As observed before, a strong coupling between cells ($T < T_c$) leads to the generation of populations with large homogeneous domains, with the same probability of finding populations mostly in red or green state (Fig. S7b). This explains the great variability observed in the average Hamming distance below the critical value of T (Fig. S7c). Interestingly, the smallest average Hamming distance was found with respect to simulated populations close to the critical value of T (Fig. S7c). These results suggest that the patterns observed in ferromagnetic colonies of spherical cells are similar to simulated populations near the critical transition, at which spatial correlations increase.

To demonstrate that the patterns observed in colonies depend on the coupling signals, we also studied colonies in which red and green states were determined by constitutive expression promoters without chemical coupling between SGNs. These states were located in plasmids that irreversibly segregate to daughter cells after cell division (Nunez *et al* (2017)), enabling cells to acquire one of the two states perpetually and creating state domains that only enlarge by cell division. Unlike the patterns observed in ferromagnetic and anti-ferromagnetic colonies, these colonies exhibited radial domains of segregating sectors such as those observed in (Rudge *et al* (2013)) (Fig. S8). Next, to test whether the observed patterns depend on the internal genetic switch module, we grew ferromagnetic colonies in the presence of IPTG and aTc to inhibit the action of LacI and TetR repressors, respectively. These colonies exhibit only one state, corresponding to the inactive repressor, whereas inhibiting both repressors led cells to adopt the state dictated by the coupling signals they sense (Fig. S9). These findings suggest that the observed ferromagnetic and antiferromagnetic patterns are the result of coupled and bi-stable gene networks.

bioRxiv preprint doi: https://doi.org/10.1101/2023.05.10.540292; this version posted May 11, 2023. The copyright holder for this preprint (which was not certified by peer review) is the author/funder, who has granted bioRxiv a license to display the preprint in perpetuity. It is made available under aCC-BY-NC-ND 4.0 International license.

Spatial correlations, cluster size distributions and critical exponents of ferromagnetic and anti-ferromagnetic colonies

To quantitatively compare the patterns generated in ferromagnetic and anti-ferromagnetic colonies of rod-shaped and spherical cells, we calculated the spatial autocorrelation function (sACF) (Walter (2017)) (Fig. 4a). The sACF describes how the correlation between two microscopic variables (e.g. the state of each cell in a colony) changes on average as the separation between these variables changes (Nounou and Bakshi (2000)), allowing the calculation of the characteristic size of the cellular state domains that emerge in a colony.

In rod-shaped and spherical cells, the correlation function curve decays much faster for anti-ferromagnetic colonies (Fig. 4a, b), suggesting that the average distance at which two cellular states correlates is shorter in these colonies. Individual colony analysis revealed that most of these colonies show negative values on the correlation curve, indicating the existence of short-range anti-correlations (insets of Fig. 4a and b). To obtain the characteristic size of the cellular state clusters, we fitted the exponential decay equation $y = y_0 * \exp(-x/b) + C$ to the data obtained from the computation of the sACF. In this equation, b correspond to the length constant, which is an estimation of the mean size of cellular state clusters that emerge in the colonies. As suggested by the patterns observed in the colonies (Fig. 3), the mean size of the cellular state domains that emerge in ferromagnetic colonies is larger than those observed in anti-ferromagnetic colonies (Table 1). This difference was independent of the reporter vector (R.V.) used. In colonies of rod-shaped cells, the mean size of the clusters in ferromagnetic colonies is approximately 8.1 (R.V.1) and 7.7 (R.V.2) times larger than the mean size in anti-ferromagnetic colonies, while in colonies of spherical cells is approximately 6.7 (R.V.1) and 6.6 (R.V.2) times larger. These results show that the ferromagnetic system leads to larger spatial correlations than those generated by the anti-ferromagnetic system.

Table 1: **Length constants of ferromagnetic and anti-ferromagnetic colonies of rod-shaped and spherical *E. coli* cells**

	Anti-ferromagnetic		Ferromagnetic	
	R.V.1	R.V.2	R.V.1	R.V.2
Rod-shaped	1.96 ± 0.54	1.85 ± 0.38	15.82 ± 2.86	14.21 ± 2.83
Spherical	2.23 ± 0.46	2.12 ± 0.62	15.05 ± 5.11	14.06 ± 3.87

Values correspond to the mean $\pm$ the standard deviation (in μm) of the sACF of around 40 colonies for each system.

Interestingly, no significant differences were found between the length constants of ferromagnetic colonies of rod-shaped and spherical cells (P value: 0.0557 for F1 rod vs F1 sph and 0.4303 for F2 rod vs F2 sph) (Fig. S10; Table 1), despite their different qualitative appearance (Fig. 3). This suggests that the spatial correlation that emerges from ferromagnetic SGNs is independent of cell shape and the mechanically-driven cell ordering. To further study the robustness of these patterns, we tested whether cell division rate affects the correlation length of Ising-like colonies. CPIM simulations predicted no significant differences in the length constants when the birth rate decreases up to 0.85 (P value: 0.3049 for 1.00 vs 0.95, 0.0650 for 1.00 vs 0.90, 0.2037 for 1.00 vs 0.85, 0.0391 for 1.00 vs 0.80, 0.0117 for 1.00 vs 0.75, < 0.0001 for 1.00 vs 0.70, < 0.0001 for 1.00 vs 0.65, < 0.0001 for 1.00 vs 0.60) (Fig. S11 a), point at which population size has decreased to approximately 70% (Fig. S11 b). To test this model prediction, we analyzed spatial correlations in colonies of spherical ferromagnetic and anti-ferromagnetic cells grown in minimal solid medium supplemented with glucose or glycerol as the carbon source. It has been observed that the generation time of *E. coli* cells increases when grown in a glycerol-supplemented medium compared to cells grown in a glucose-supplemented medium (Taheri-Araghi *et al* (2015)). In agreement with the CPIM predictions, length constants were no significantly affected in ferromagnetic and anti-ferromagnetic colonies that had reduced their size more than half (P value cluster size: 0.1453 for Glu vs Gly Ferro, 0.7395 for Glu vs Gly Anti-ferro; P value colony size: < 0.0001 for Glu vs Gly Ferro, < 0.0001 for Glu vs Gly Anti-ferro) (Fig. 4c). Together, these results suggest that the scaling properties of Ising-like, bi-stable and coupled SGNs are independent of the cell shape and division rate.

To further characterize the behaviour of the ferromagnetic system, we analyzed the size distribution of

bioRxiv preprint doi: https://doi.org/10.1101/2023.05.10.540292; this version posted May 11, 2023. The copyright holder for this preprint (which was not certified by peer review) is the author/funder, who has granted bioRxiv a license to display the preprint in perpetuity. It is made available under aCC-BY-NC-ND 4.0 International license.

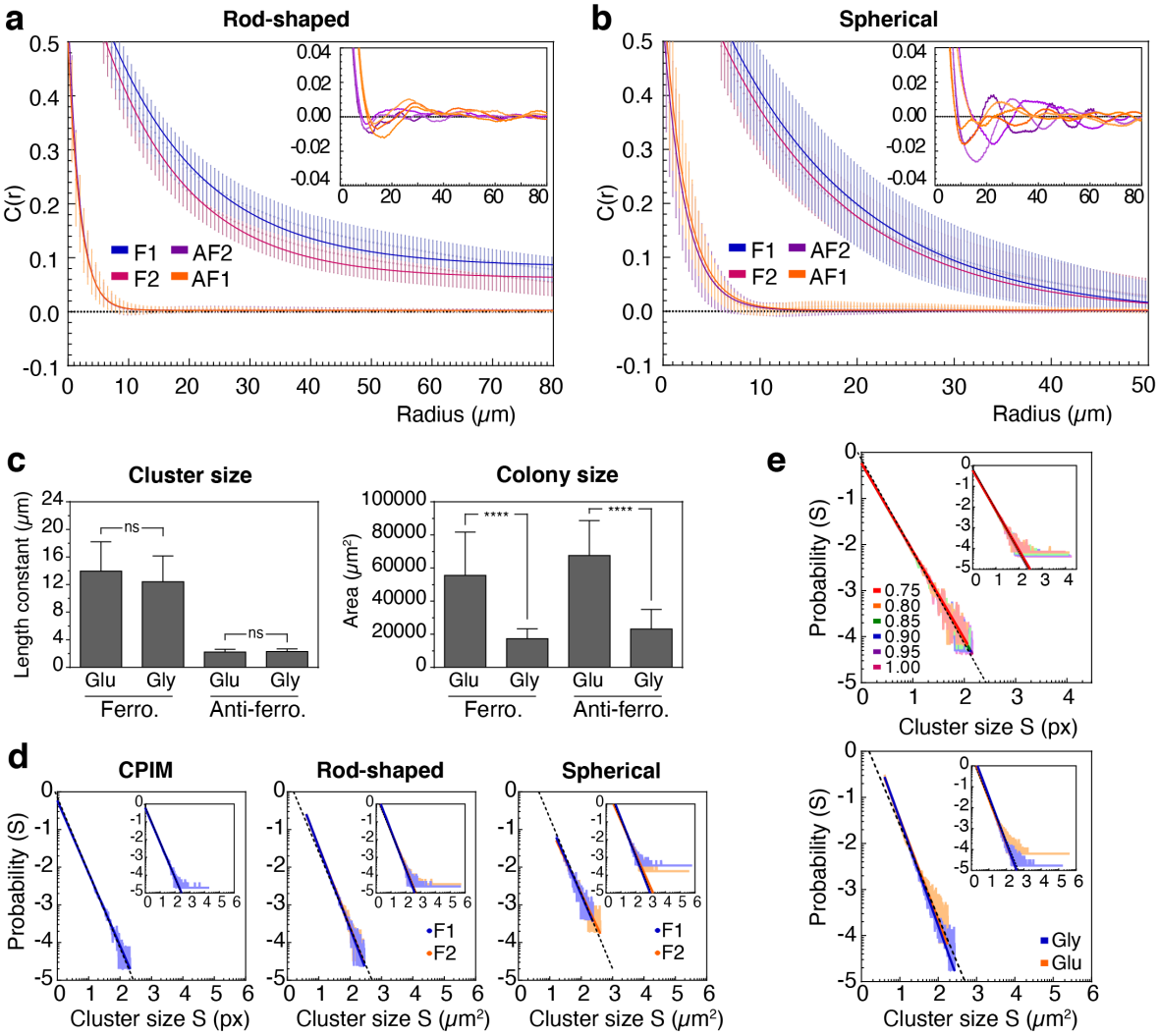

Figure 4: **Spatial correlation in ferromagnetic and anti-ferromagnetic colonies.** Spatial autocorrelation function $C(r)$ in colonies of rod-shaped (a) and spherical (b) *E. coli* cells carrying the ferromagnetic (F) and anti-ferromagnetic (AF) systems with reporter vector 1 (F1 and AF1) or 2 (F2 and AF2). Points and error bars correspond to the mean ± the standard deviation of around 40 colonies for each system, and lines correspond to the best fit of the exponential decay equation $y = y_0 * \exp(-x/b) + C$ to the data. Insets show the oscillating behaviour of the sACF around zero of individual anti-ferromagnetic colonies, which is lost when the data is averaged. (c) Length constant and colony size of ferromagnetic and anti-ferromagnetic colonies of spherical *E. coli* cells grown in M9 solid medium supplemented with glucose (Glu) or glycerol (Gly), showing that cell division rate does not affect the spatial correlations. Statistical analysis was performed using two-tailed Mann-Whitney test ($\alpha = 2.5\%$). ns (not significant): $P > 0.05$; $****$: $P \leq 0.0001$. (d) Probability distribution $P(S)$ ($\log_{10} - \log_{10}$ plots) of the cluster size S (in pixels) for ferromagnetic populations simulated with CPIM (left) and ferromagnetic colonies of rod-shaped (middle) and spherical (right) cells. (e) Probability distribution of the cluster size for ferromagnetic populations simulated with CPIM at different cell birth rates, from 0.75 to 1.00 (top), and ferromagnetic colonies of spherical cells grown in glycerol (blue) or glucose (red) (bottom). Plots in (d) and (e) were obtained using the algorithms r_plfit with the default low frequency cut-off Hanel *et al* (2017). Solid lines correspond to the power-law $P(s) = Cx^{-\gamma}$ found by the algorithm. Insets show the probability distribution of all the clusters found in the populations (without cut-off), with solid lines corresponding to the best fit of the data to equation $P(s) = A * s^{-\gamma}$ found by the least squares method. Doted lines correspond to a curve with $\gamma = 2.00$.

bioRxiv preprint doi: https://doi.org/10.1101/2023.05.10.540292; this version posted May 11, 2023. The copyright holder for this preprint (which was not certified by peer review) is the author/funder, who has granted bioRxiv a license to display the preprint in perpetuity. It is made available under aCC-BY-NC-ND 4.0 International license.

the cellular state clusters. As seen in Figure 4d, the probability distribution $P(S)$ of cluster size S for ferromagnetic colonies of rod-shaped and spherical cells shows a scale invariant distribution of the form $P(s) \sim s^{-\gamma}$. The values of γ calculated for the ferromagnetic systems are consistent with the exponent of cluster size distribution near the critical percolation threshold, which follows a power-law decay with an exponent of 2.055 (Stauffer and Aharony (1994)) (Rod-shaped: R.V.1 = 2.17, R.V.2 = 2.14. Spherical: R.V.1 = 1.91, R.V.2 = 1.76) (Table S5). This exponent was also consistent with the value of γ for simulated populations with ferromagnetic interactions at $T = T_c$ ($\gamma = 1.93$). Interestingly, the simulations also showed that the size distribution of cellular state clusters is not affected by changes in the birth rate (Fig. 4e) (Table S6). As predicted by CPIM simulations at different cell growth rates, similar power law distributions were found for ferromagnetic colonies grown in glycerol or glucose, with scaling exponent γ equal to 2.19 for glucose and 2.31 for glycerol(Fig. 4e) (Table S5). This suggests that the scaling properties are maintained upon changes in cell growth rate within the evaluated range.

Discussion

Understanding how gene spatial correlations emerge from interacting genetic networks is a fundamental problem in biology. Guided by a contact process lattice model with Ising mechanisms, we show how synthetic gene networks with two states, which are positively or negatively coupled, give rise to a rich repertoire of short- and long-range correlations (and anticorrelations). These SGNs are capable of self-organizing into long-range correlations with power-law scaling properties or checkerboard-like patterns similar to ferromagnetic and anti-ferromagnetic configurations of the Ising Model near critical points, respectively. Near the critical point, the spatial autocorrelation function of simulated ferromagnetic populations follows a power-law decay with an exponent consistent with the value of the Ising model at the critical temperature. On the other hand, the scaling exponent γ calculated for both simulated and *in vivo* ferromagnetic colonies were close to the exponent of the cluster size distribution near the critical percolation threshold (Larkin *et al* (2018); Stauffer and Aharony (1994)). At this critical point, the system moves from a regime of only localized short-range patches to one with clusters that span the entire system. These results suggest that the ferromagnetic system can pose colonies near the critical point of phase transition in which far regions in the colony are correlated. These findings are in agreement with the work of Weber and Buceta, who found that simulations of toggle switches with coupled states can exhibit phase transitions described by the theory of critical phenomena (Weber and Buceta (2016)). Although our results suggest that the behavior of these SGNs could belong to the Ising universality class (Ibarra-García-Padilla *et al* (2016); Goldenfeld (1992)), the lack of a control parameter, equivalent to temperature or the coupling interaction exchange J, in the *in vivo* experimental system limits the search for universal critical exponents. Such control parameter could be realized *in vivo* by the regulation of coupling signal levels outside the cells or their transport rate across the cell membrane (Weber and Buceta (2016)).

This work shows how two-state switches with different coupling mechanisms can lead to spatial patterns of rich scaling properties in isogenic bacterial populations. Microbes are constantly adjusting their metabolism to changing environments, and even clonal populations can become spatially structured, giving rise to interacting metabolic subpopulations shaped by cellular uptake and release of coupling compounds (Dal Co *et al* (2019); Rosenthal *et al* (2018); Cole *et al* (2015)). Whether local metabolic couplings (e.g. Shapiro (1998); Blanchard and Lu (2015); Mee *et al* (2014); Cole *et al* (2015); Rosenthal *et al* (2018); Liu *et al* (2015); Dal Co *et al* (2020)) can lead to Ising-like patterns in natural multicellular systems remains to be explored. This work provides a minimal system to address these questions as well as other fundamental problems in developmental and microbiology, such as phase transition and symmetry breaking (Weber and Buceta (2016)), with promising applications for the engineering of pattern formation, synthetic bacterial consortia and artificial morphogenesis (Nguyen *et al* (2018); Teague *et al* (2016); Johnson *et al* (2017); Santos-Moreno and Schaerli (2019); Ebrahimkhani and Levin (2021); Davies and Glykofrydis (2020); Bittihn *et al* (2018); Solé *et al* (2018)).

bioRxiv preprint doi: https://doi.org/10.1101/2023.05.10.540292; this version posted May 11, 2023. The copyright holder for this preprint (which was not certified by peer review) is the author/funder, who has granted bioRxiv a license to display the preprint in perpetuity. It is made available under aCC-BY-NC-ND 4.0 International license.

Materials and methods

Computational modeling

The code for the simulation of the Ising model during the growth of a bacterial colony was written in the C programming language, and it is available in Github `https://github.com/kevinsimpson12/CP-IM`. The graphical user interface was created with GTK+ 3 (`https://developer.gnome.org/gtk3/stable/`).

Plasmids

All the vectors used in this work, listed in Table S1, were constructed by Golden Gate (Engler *et al* (2008)) and Gibson Assembly (Gibson *et al* (2009)). Level 0 modules used in the Golden Gate assembly containing one of the four genetic elements that are part of a Transcriptional Unit (promoter, Ribosome Binding Site RBS, coding sequence, and terminator), were either obtained from the CIDAR MoClo kit (Iverson *et al* (2016)) deposited in Addgene (Kit #1000000059) or constructed by Gibson Assembly using gBlocks supplied by IDT (idtdna.com). The pLux76pTet and pLas81pLac double promoters designed in this work were synthesized based on the sequences of pLux76 and pLas81 promoters used in (Grant *et al* (2016)). The sequence of *mCherry2* was obtained from (Shen *et al* (2017)). Different Level 1 vectors containing Transcriptional Units were generated by Golden Gate combining different Level 0 modules. Four of these Level 1 Transcriptional Units were combined together by Gibson Assembly to generate the Level 2 reporter and Ising vectors. PCR fragments used in the Gibson Assembly were amplified using Phusion High-Fidelity DNA Polymerase (NEB) and were visualized on a blue LED transilluminator (iorodeo.com) using SYBR Safe (Thermofisher). The purification of the vectors was performed using the Wizard Plus SV Minipreps DNA Purification System (Promega), while the purification of the PCR fragments was performed using the Wizard SV Gel and PCR Clean-Up System (Promega).

Bacterial strains and Growth conditions

All experiments were performed using the *E. coli* TOP10 (Invitrogen) or KJB24 strains. KJB24 strain contains a stop codon mutation in the cell wall protein RodA, which results in the generation of spherical cells, and a second mutation that allows cells to grow in rich medium (Begg and Donachie (1998)). To transform cells with Ferromagnetic and Antiferromagnetic systems, cells of TOP10 and KJB24 strains were made competent by the CCMB80 method (`http://openwetware.org/wiki/TOP10_chemically_competent_cells`). Cells were grown on LB liquid medium (tryptone 10 g, yeast extract 5 g, NaCl 5 g, and distilled water to a final volume of 1 L) or on M9-glucose liquid medium (1x M9 salts supplemented with $MgSO_4{*}7H_2O$ 2 mM, $CaCl_2$ 0.1 mM, glucose 0.4% and casamino acids 0.2%, where 1 L of 5× M9 salts contains 64 g of $Na_2HPO_4{*}7H_2O$, 15 g of KH_2PO_4, 2.5 g of NaCl, and 5 g of NH_4Cl), where 1.5% w/v agar was added to the corresponding liquid medium to prepare LB agar or M9-glucose agar medium. When necessary, the medium was supplemented with 50 μg/mL kanamycin, 100 μg/mL carbenicillin, 50 μg/mL spectinomycin or 10 μg/mL chloramphenicol. In order to prepare the stock solutions of acyl-homoserine lactone molecules, 3-oxohexanoyl-homoserine lactone (C6HSL, Cayman Chemicals) and 3-oxododecanoyl-homoserine lactone (C12HSL, Sigma) were dissolved in DMSO to a concentration of 0.067 M. Before being used, both acyl-homoserine lactones were first diluted in ethanol to a concentration of 2 mM, and then diluted in M9-glucose medium to the described concentrations. To obtain images of colonies, cells were grown overnight at 37 °C in liquid M9-glucose medium and diluted 1:100 in the same fresh liquid medium. Cells were then grown to an optical density at 600 nm of 0.2, diluted 1:1000 and 20 μL of these dilutions were plated onto M9-glucose agar plates with the appropriate antibiotic and the described concentrations of C6HSL. To compare the effects of growth rate in the emergence of patterns, cells were also plated onto M9-glycerol agar plates, in which the glucose was replaced with 0.2% glycerol.

Plate fluorometry

Cells were grown overnight in a shaking incubator at 37 °C in 4 ml of liquid M9-glucose medium supplemented with the appropriate selective antibiotics. The overnight cultures were diluted 1:1000 in the same fresh liquid medium, and 200 μl of these dilutions were transferred into a well of a 96-well clear-bottom plate and

bioRxiv preprint doi: https://doi.org/10.1101/2023.05.10.540292; this version posted May 11, 2023. The copyright holder for this preprint (which was not certified by peer review) is the author/funder, who has granted bioRxiv a license to display the preprint in perpetuity. It is made available under aCC-BY-NC-ND 4.0 International license.

supplemented with the described concentration of C6HSL or C12HSL. The plates were placed in a Synergy HTX plate reader (BioTek) and fluorescence (sfGFP: 485/20 nm excitation, 516/20 nm emission; mCherry2: 585/10 excitation, 620/15 nm emission) and optical density (600 nm) were measured every 10 min for 24 hours. The plates were maintained at 37 °C during the experiment and were shaken at 200 rpm between readings.

Microscopy and Image analysis

A Nikon Ti microscope equipped with 10x, 20x and 40x objectives, and FITC and TRITC Filter Cube Sets was used to obtain the images of the colonies. Images were acquired using the Nikon NIS-Elements BR software. The processing and analysis of the images was performed using the Fiji distribution of ImageJ (Schindelin *et al* (2012)). Single-channel images of the colonies were created by merging a z-stack using the Extended Depth Field pluging, while multi-channel images were merged using the Merge command. Before the analysis of the images, single-channel images were converted into 8-bits, the background was removed using the Subtract Background command and the images were binarized using the Automatic Threshold pluging. To investigate the existence of a characteristic spatial distribution of the cellular-state domains, we used the AutoCorrelation Function (ACF) pluging (Walter (2017)) (`https://github.com/vivien-walter/autocorrelation`) to calculate the spatial Autocorrelation Function (sACF) of binarized images of whole colonies. A value of 1 or -1 of the sACF means a perfect correlation or anticorrelation, respectively, while a value of 0 means no correlation. To calculate the mean size of the cellular state clusters generated in the colonies we used Gnuplot (`http://www.gnuplot.info/`) to fit the data of the sACF to the one phase exponential decay equation $y = y_0 * \exp(-x/b) + C$, where b is the length constant, which correspond to the average size of the cellular states domains generated in the colonies.

To obtain the probability distribution of cluster sizes, we calculate the number and size of the clusters of binarized images of colonies and simulations using the Find Connected Regions Plugin of ImageJ (`http://homepages.inf.ed.ac.uk/s9808248/imagej/find-connected-regions/`). The values of the power-law exponents γ were estimated by finding the best fit for all the data using the least squares method and also using the matlab implementation of the algorithm r_plfit(k,'hist') developed by Hanel et al. with default low frequency cut-offs (Hanel *et al* (2017)). For the colonies, only clusters greater than 1 μm were considered for the analysis.

To determine the similarity between ferromagnetic colonies and ferromagnetic populations obtained from CPIM simulations, we calculate the Hamming distance using a custom Python program that determines the number of pixel positions in which the images are different. Binarized images of both colonies and simulations were scaled to have the same number of pixels, saved as a binary array in a text file, and the Python program was used to compare each position in the array (which represents a pixel of the binarized image) of two images. If in that position both images have the same pixel value, the program adds a 0, but if the values are different, the program adds a 1. The total number of pixels in which the images are different is then divided by the total number of pixels to obtain the Hamming distance. For this analysis, 42 colonies of ferromagnetic cells with the reporter vector 1 and 65 colonies of ferromagnetic cells with the reporter vector 2 were compared with 10 simulated population for each value of the control parameter between 2 and 2.54. To find the smallest value of the Hamming distance between a colony and a simulated population, the image of the simulated population was rotated every 15 degrees, generating a total of 24 versions for each simulated population. Thus, the final value of the Hamming distance corresponds to the smallest value obtained from the calculation of the distance between the colony and each version of the simulated population. One-way ANOVA followed by Dunnett's multiple comparisons test, and non parametric, two-tailed Mann-Whitney test ($\alpha = 2.5\%$) were performed using GraphPad Prism for Windows, GraphPad Software, San Diego, California USA, `http://www.graphpad.com`.

All the raw data is available in an open data repository in Zenodo (`https://doi.org/10.5281/zenodo.7047215`).

Acknowledgements

K.S. was supported by Beca de Doctorado Nacional CONICYT 2016 (21160554); J.K. was supported by ANID – Núcleo Milenio Física Materia Activa - Iniciativa Científica Milenio and ANID Fondecyt Regular

bioRxiv preprint doi: https://doi.org/10.1101/2023.05.10.540292; this version posted May 11, 2023. The copyright holder for this preprint (which was not certified by peer review) is the author/funder, who has granted bioRxiv a license to display the preprint in perpetuity. It is made available under aCC-BY-NC-ND 4.0 International license.

1191893; F.F. was supported by ANID – Millennium Science Initiative Program – ICN17_022 and ANID Fondecyt Regular 1211218. We thank Tim Rudge, Janneke Noorlag, Peter Galajda, Miles Wetherington, Anton Kan and members of F.F. group for valuable comments and feedback.

Author Contributions

K.S. performed experiments and analyzed data. J.K and F.F acquired funding and supervised the project. The three authors wrote and edited the manuscript.

Supporting information

Simulation of the Ising model during the growth of a population

To study the effects of Ising-like interactions in a growing population of cells, we created a lattice model that combines cell population dynamics and Ising rules for cell state differentiation. We combined the simulation of the two-dimensional Ising model, using the Metropolis algorithm Metropolis *et al* (1953), with the Contact Process lattice model Harris (1974) to represent cell population dynamics. We name this model CPIM (Contact Process - Ising Model). CPIM consists of an interacting particle system which follows colonization, extinction and differentiation dynamics of particles on a two-dimensional lattice ($\mathcal{L}$) of N sites. Each site of this lattice can be in one of four states $S = \{\varnothing, *, -1, +1\}$, which represent vacant locations ($\varnothing$, white squares), locations occupied with undifferentiated cells ($*$, black squares), and locations occupied with differentiated cells in red ($+1$, red squares) or green (-1, green squares) state. The state of a site x at a time t can be described as $\xi_t(x)$. Thus, an interacting particle system $\xi_t : \mathcal{L} \to S$ (that assign one state from S to all sites in the lattice) is determined by the following lattice reactions from two set of processes:

i) Birth, death, colonization and differentiation processes: cells can die or survive at rates δ and b, respectively. If they survive, they divide and give birth to daughter cells that can occupy only nearest (north, south, east and west) vacant sites in the lattice, originating an advancing front of growing cells that colonizes available habitat in the landscape. This spatial spread is represented by $\varnothing_x + *_y \to *_x + *_y$, while cell death is represented by $*_x \xrightarrow{\delta} \varnothing_x$. Colonization only occurs between nearest neighbours $\|x - y\| \leq 1$ for x, y representing sites on the lattice $\mathcal{L}$. At the beginning of the simulation, an undifferentiated cell is placed in the center of the lattice. Then, a site on the lattice is randomly selected, and if this focal site is vacant, a random neighbour is selected. If this neighbour of the focal site is occupied, it colonizes the vacant site with probability 1. On the other hand, if the focal site is occupied by a undifferentiated cell ($*$), it can differentiate into a red ($+1$) or green (-1) state at a certain rate α, which is represented by $*_x \xrightarrow{\alpha} +1_x$ and $*_x \xrightarrow{\alpha} -1_x$. These differentiated cells can also die or give birth to daughter cells with the same rates δ and b.

ii) Ising-like cellular states alignment process: To determine if differentiated cells can change from one state to another (red to green or green to red), a site in the lattice occupied by a differentiated cell is randomly selected and the change in the interaction energy $\Delta\mathcal{H}$, which results if the state of the cell at that site is changed, is calculated using the Eq 1. The notation $\langle ij \rangle$ in this equation indicates that the sum is between neighbouring pairs of cells, allowing only a short-range interaction between cells. For the interaction energy calculations, we assumed that $J = +1$ for ferromagnetic systems and $J = -1$ for anti-ferromagnetic systems. This assumption implies that the interaction energy between neighbouring cells is minimized when they have the same state in a ferromagnetic system, or the opposite state in an anti-ferromagnetic system (Eq. 1). Thus, if $\Delta\mathcal{H} < 0$, the change in the state is accepted since this change decreases the total energy of the system. If $\Delta\mathcal{H} \geq 0$, which means an increase in the total energy of the system, the change in the state is accepted only if $r < e^{-\Delta\mathcal{H}/k_B T}$, where r is a random number such $0 < r < 1$ Landau and Binder (2014). In the classical Ising model, T is the absolute temperature, and correspond to the control parameter of the system. This means that varying T determines the transition between ordered and disordered configurations of the system. In our model T represents a parameter that determines the coupling strength between cells in the system: a small value of T represents a strong coupling, while a large value represents a weak coupling.

In this model, one generation time corresponds to the moment when all the sites in the lattice have had the possibility of being visited. In a 250x250 lattice, we run simulations for 200 generation times. It is also important to note that a lattice site in the CPIM simulations can have two interpretations. As described

bioRxiv preprint doi: https://doi.org/10.1101/2023.05.10.540292; this version posted May 11, 2023. The copyright holder for this preprint (which was not certified by peer review) is the author/funder, who has granted bioRxiv a license to display the preprint in perpetuity. It is made available under aCC-BY-NC-ND 4.0 International license.

above, a lattice site in the CPIM simulations can represent a cell. However, a lattice site in this model can also represent a cell territory. Considering lattice sites as cell territories is particularly relevant since it allows to map a lattice site to a sector in a colony. In this interpretation, beside considering lattice sites as cell territories (and not individual cells), the death rate represents the clearance rate of territories, and the division/birth rate represents the local colonization rate. However, the usefulness of the model remains the same: local interactions can give rise to large scale order.

bioRxiv preprint doi: https://doi.org/10.1101/2023.05.10.540292; this version posted May 11, 2023. The copyright holder for this preprint (which was not certified by peer review) is the author/funder, who has granted bioRxiv a license to display the preprint in perpetuity. It is made available under aCC-BY-NC-ND 4.0 International license.

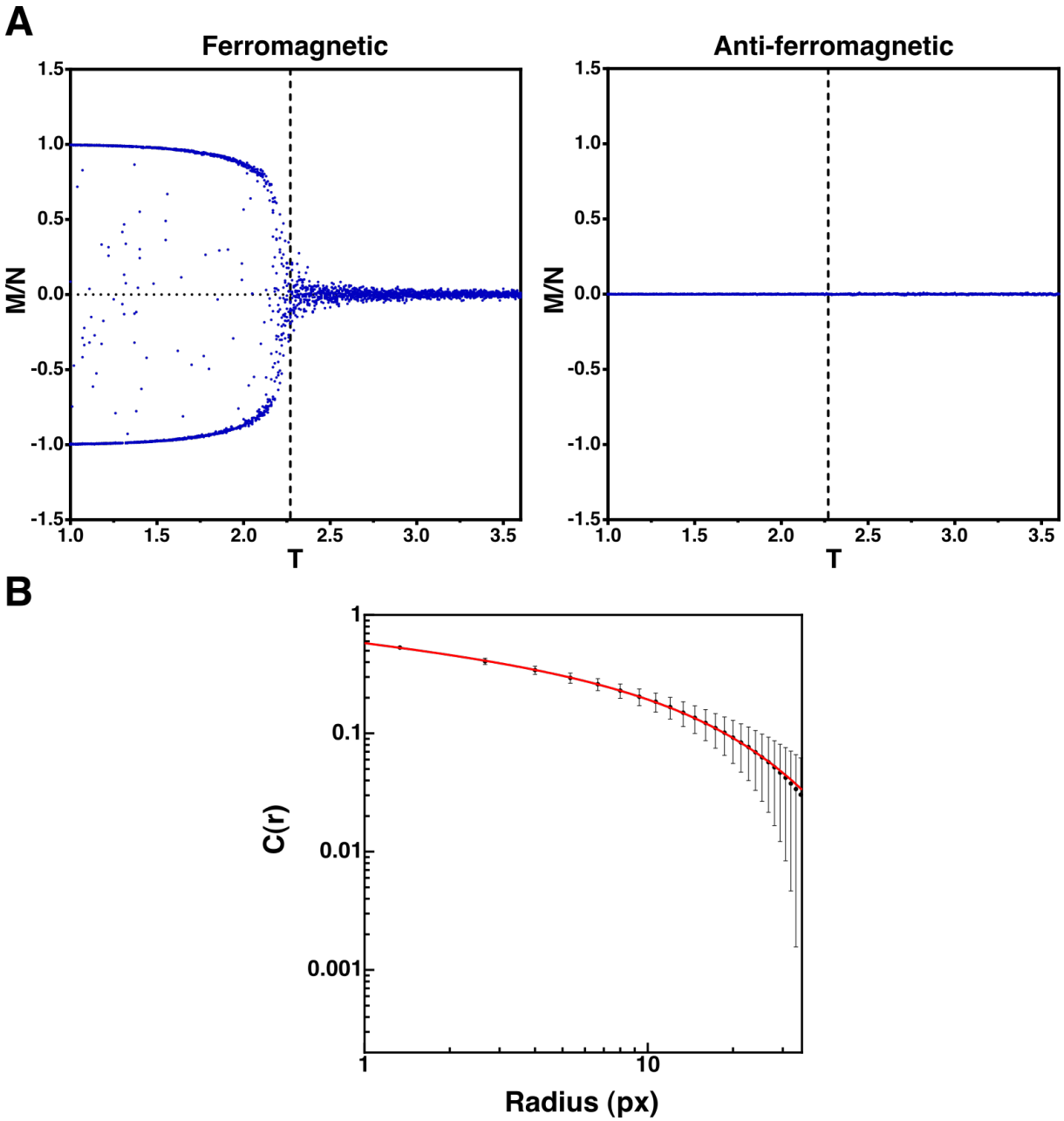

Figure S1: **Power-law decay of the sACF in ferromagnetic populations simulated using the lattice model.** (A) Magnetization per site M/N as a function of T for ferromagnetic and anti-ferromagnetic populations simulated with the CPIM model. Dotted vertical lines mark the critical value of T (T_c). Below T_c, most cells have the same cellular state due to the strong coupling, and the value of $|M|$ is close to 1. Above T_c, cells can randomly adopt a cellular state independent of the state of their neighbors, and the value of $|M|$ is close to 0. The value of M for a population with anti-ferromagnetic interactions showed to be always close to zero, independent of the value of T. 10 simulations per each value of T were used. (B) sACF of simulated populations with ferromagnetic interactions at the critical value of T ($T = T_c$). The sACF showed to follow a power-law decay with a critical exponent $\eta = 0.2518$. Black dots and error bars correspond to the mean $\pm$ the standard deviation of the sACF of 50 simulations at $T = T_c$, and the red line correspond to the best fit of the data to the curve $C(r) = A\frac{exp(-r/B))}{r^{\eta}}$, where η corresponds to the critical exponent of the autocorrelation function. The radius is in pixels.

bioRxiv preprint doi: https://doi.org/10.1101/2023.05.10.540292; this version posted May 11, 2023. The copyright holder for this preprint (which was not certified by peer review) is the author/funder, who has granted bioRxiv a license to display the preprint in perpetuity. It is made available under aCC-BY-NC-ND 4.0 International license.

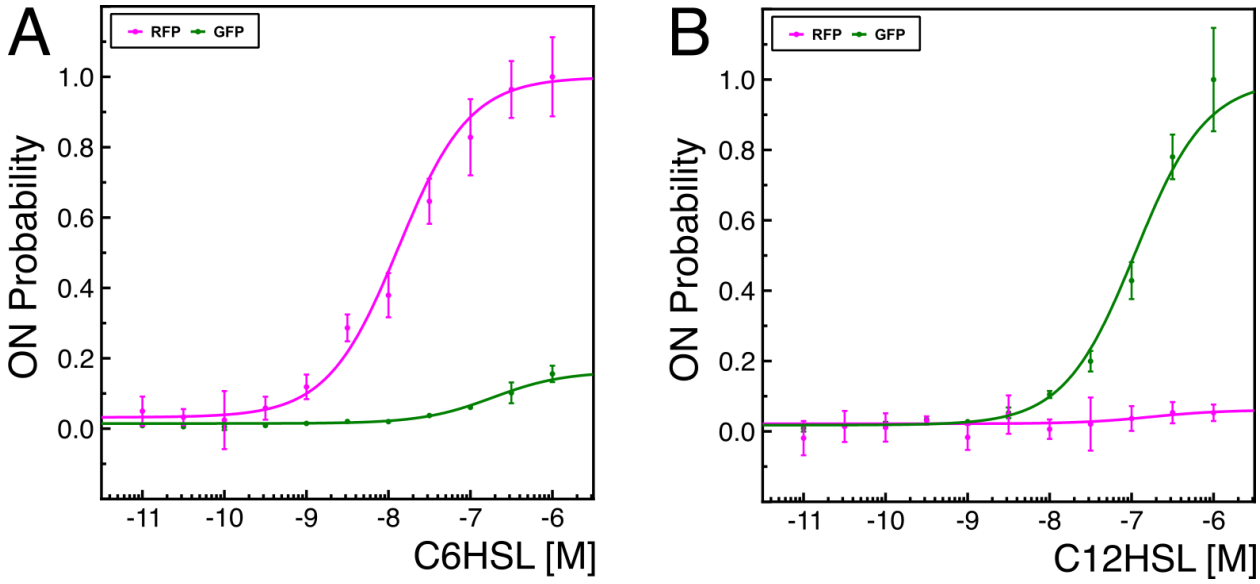

Figure S2: **Red and green fluorescent protein synthesis rate of *E. coli* cells carrying the reporter vector.** Cells were grown in liquid media supplemented with different concentrations of C6HSL (left) and C12HSL (right). Points and error bars correspond to the values of the fluorescent protein synthesis rates normalized by its maximum value reached in each system, and lines correspond to the fit of the data to Eq. 2. Values on x-axis correspond to the $\log_{10}$ of the C6HSL concentration.

bioRxiv preprint doi: https://doi.org/10.1101/2023.05.10.540292; this version posted May 11, 2023. The copyright holder for this preprint (which was not certified by peer review) is the author/funder, who has granted bioRxiv a license to display the preprint in perpetuity. It is made available under aCC-BY-NC-ND 4.0 International license.

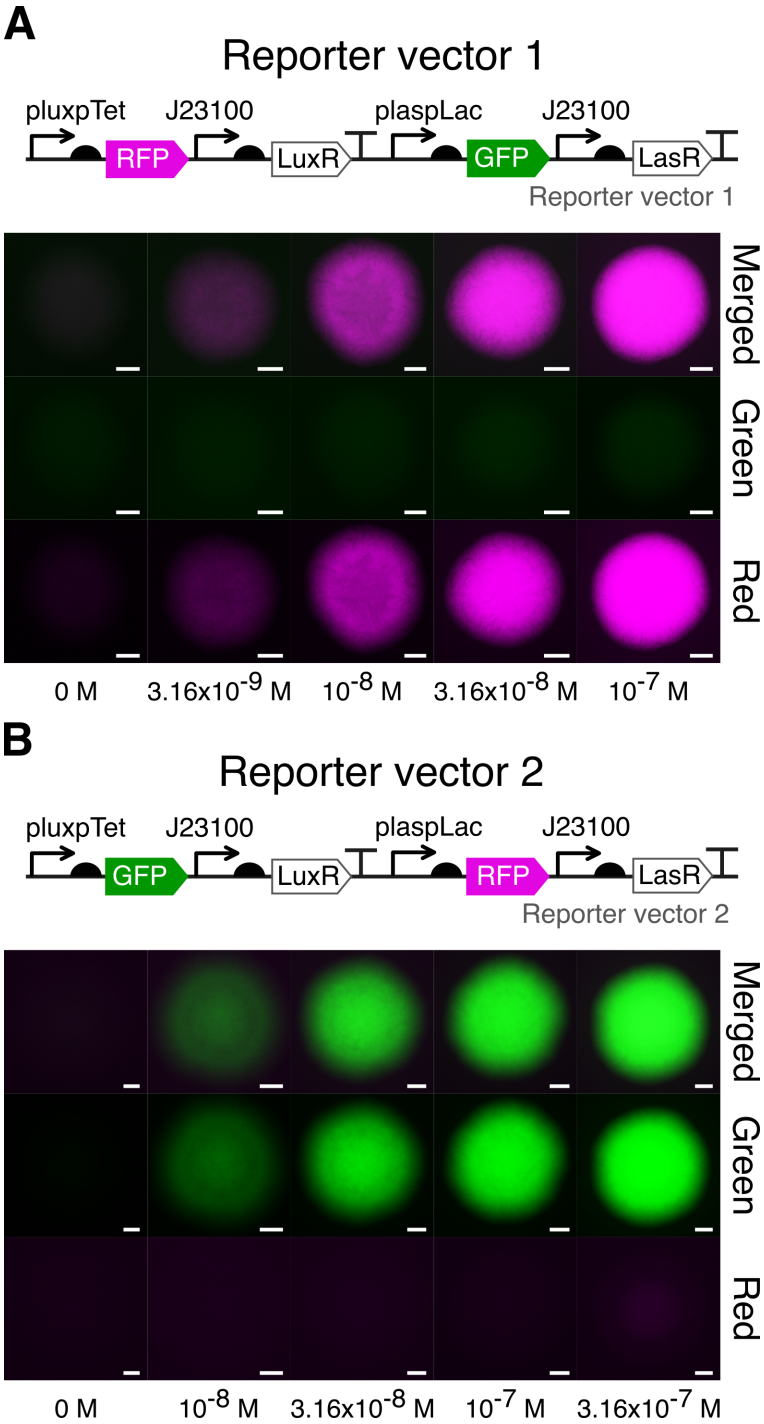

Figure S3: **Induction of red and green fluorescence by C6HSL in colonies of rod-shaped cells carrying different versions of the reporter vector.** Red and green fluorescence of colonies of cells carrying the reporter vector 1 (A) and reporter vector 2 (B) grown on solid M9-glucose media supplemented with different concentrations of C6HSL. Gene network arrangement of reporter vector 1 and 2 is included for comparison. Images were taken approximately 14 hours after inoculation. Scale bars 100 μm.

bioRxiv preprint doi: https://doi.org/10.1101/2023.05.10.540292; this version posted May 11, 2023. The copyright holder for this preprint (which was not certified by peer review) is the author/funder, who has granted bioRxiv a license to display the preprint in perpetuity. It is made available under aCC-BY-NC-ND 4.0 International license.

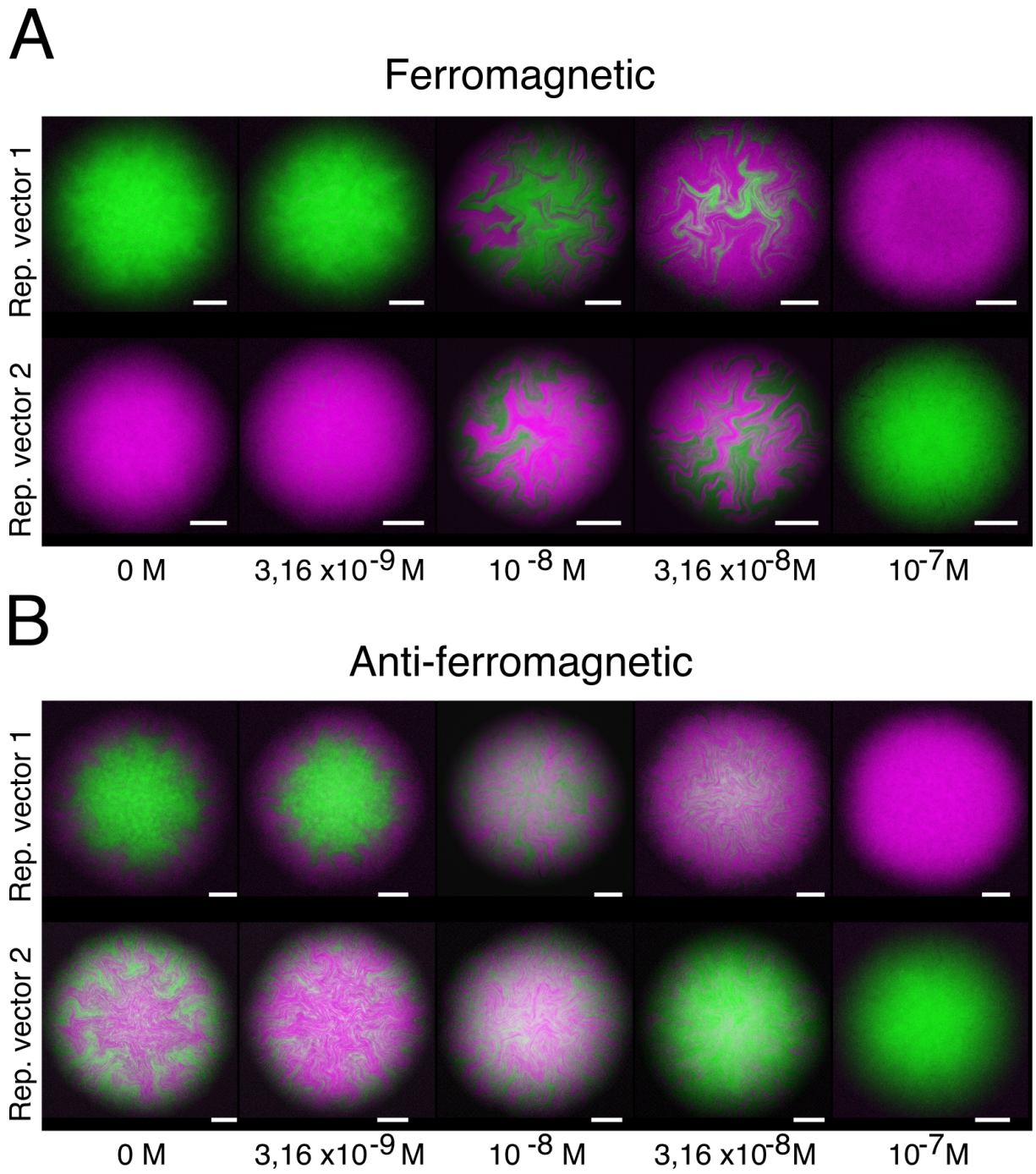

Figure S4: **Red and green state patterns generated in ferromagnetic and anti-ferromagnetic colonies at different concentration of C6HSL.** Representative images of the cellular state patterns generated in colonies of rod-shaped *E. coli* cells carrying the ferromagnetic (A) or anti-ferromagnetic (B) vector along with the reporter vector 1 or 2. Cells were grown on solid glucose-M9 media supplemented with the indicated concentration of C6HSL. Images were taken approximately 14 hours after inoculation. Scale bars 100 μm.

bioRxiv preprint doi: https://doi.org/10.1101/2023.05.10.540292; this version posted May 11, 2023. The copyright holder for this preprint (which was not certified by peer review) is the author/funder, who has granted bioRxiv a license to display the preprint in perpetuity. It is made available under aCC-BY-NC-ND 4.0 International license.

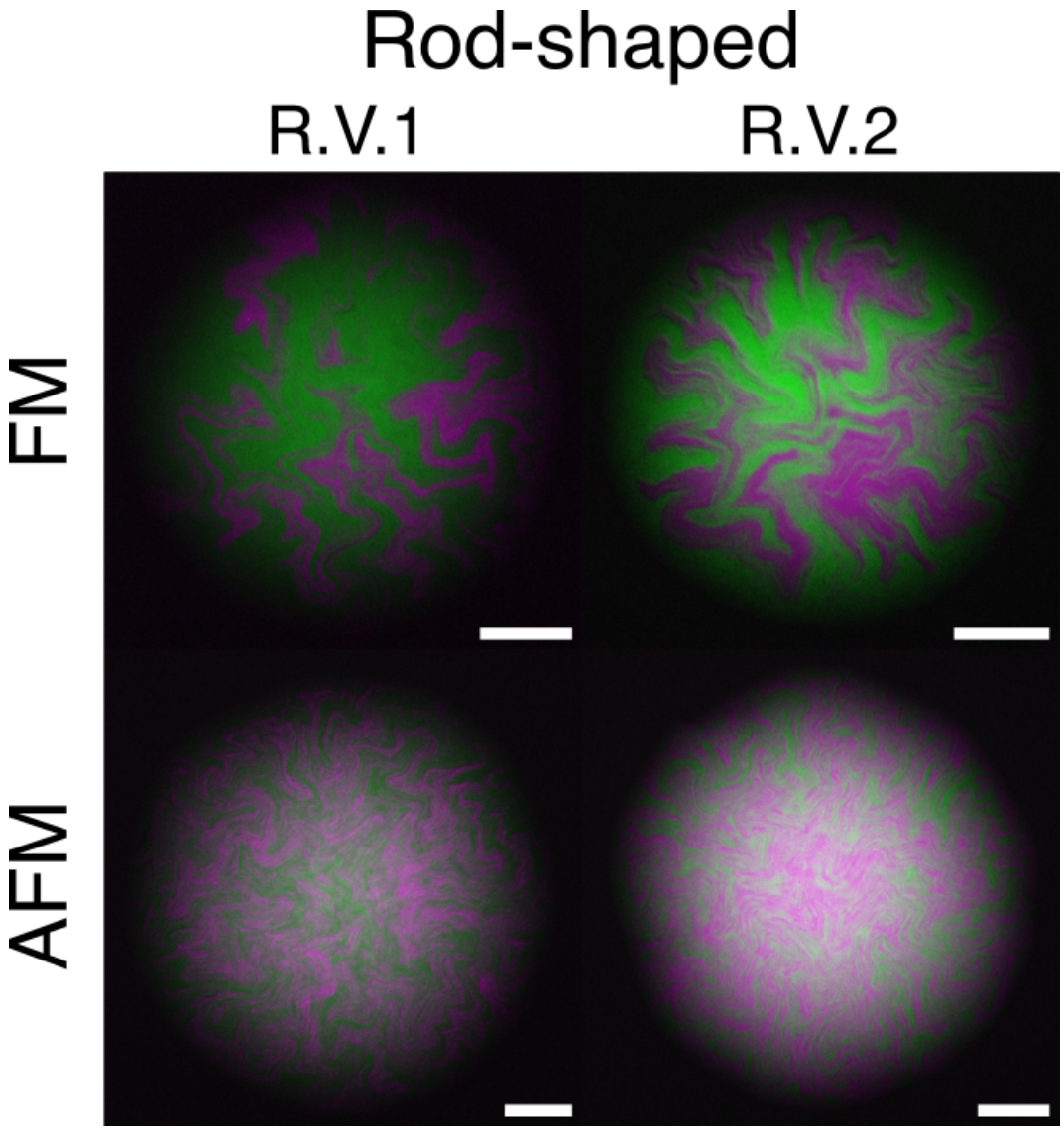

Figure S5: **Cellular state patterns in ferromagnetic and anti-ferromagnetic colonies.** Representative images of red and green fluorescent protein patterns in colonies of rod-shaped *E. coli* cells carrying the ferromagnetic (FM) or anti-ferromagnetic (AFM) systems with reporter vector 1 (R.V.1) or 2 (R.V.2). Cells were grown on solid M9-glucose medium supplemented with 10^{-8} M of C6HSL. Images were taken approximately 14 hours after inoculation. Scale bars 100 μm.

bioRxiv preprint doi: https://doi.org/10.1101/2023.05.10.540292; this version posted May 11, 2023. The copyright holder for this preprint (which was not certified by peer review) is the author/funder, who has granted bioRxiv a license to display the preprint in perpetuity. It is made available under aCC-BY-NC-ND 4.0 International license.

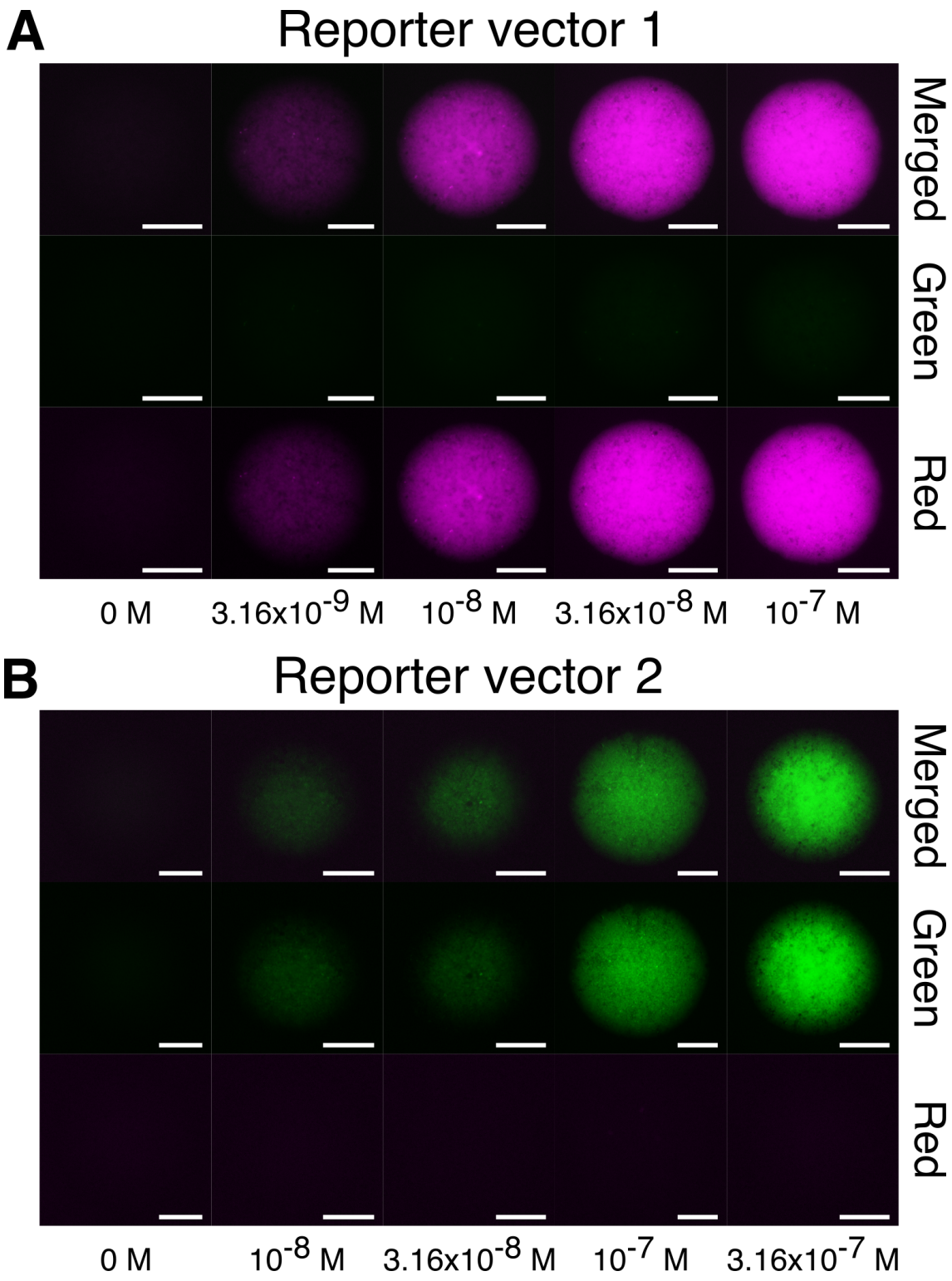

Figure S6: **Induction of red and green fluorescence by C6HSL in colonies of spherical cells carrying different versions of the reporter vector.** Red and green fluorescence of colonies generated from cells carrying the reporter vector 1 (A) and reporter vector 2 (B) grown on solid M9-glucose medium supplemented with different concentrations of C6HSL. Images were taken approximately 18 hours after inoculation. Scale bars 100 μm.

bioRxiv preprint doi: https://doi.org/10.1101/2023.05.10.540292; this version posted May 11, 2023. The copyright holder for this preprint (which was not certified by peer review) is the author/funder, who has granted bioRxiv a license to display the preprint in perpetuity. It is made available under aCC-BY-NC-ND 4.0 International license.

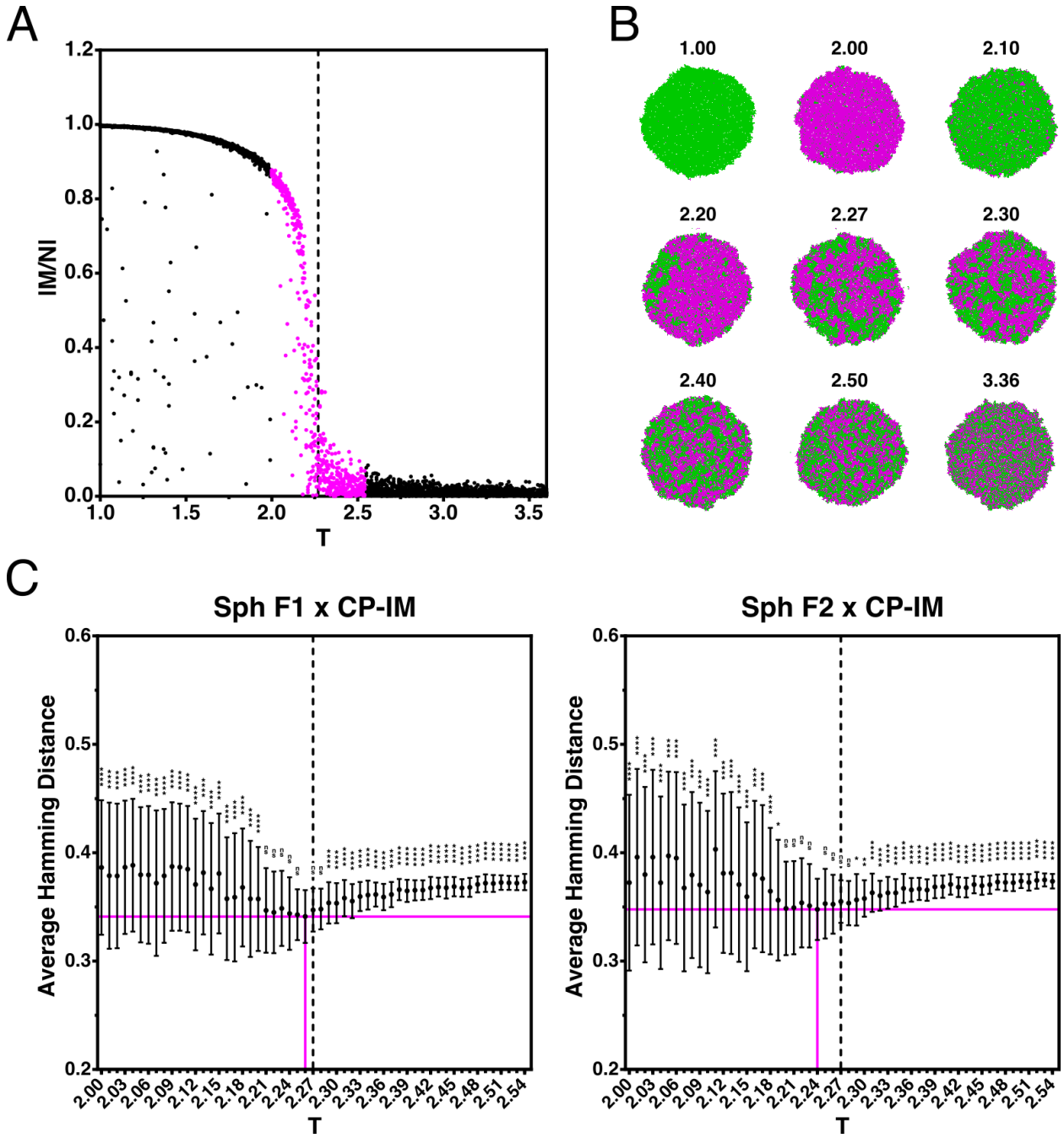

bioRxiv preprint doi: https://doi.org/10.1101/2023.05.10.540292; this version posted May 11, 2023. The copyright holder for this preprint (which was not certified by peer review) is the author/funder, who has granted bioRxiv a license to display the preprint in perpetuity. It is made available under aCC-BY-NC-ND 4.0 International license.

Figure S7: **Hamming distance between ferromagnetic colonies of spherical cells and simulated populations with the lattice model.** (A) Magnetization per site $|M/N|$ as a function of T for ferromagnetic populations simulated with the lattice model. Dotted vertical line marks the critical value of T ($T_c = 2.27$). Red dots correspond to the simulations used to calculate the Hamming distance in C. (B) Images of simulated ferromagnetic populations at different values of the control parameter T, highlighting that the probability of finding populations in the red or green state below T_c is the same. (C) Hamming distance calculated between ferromagnetic colonies of spherical (Sph) cells carrying the reporter vector 1 (left, FM1) or 2 (right, FM2) and the simulated ferromagnetic populations with the CPIM model around the T_c. Black dots and error bars correspond to the mean $\pm$ the standard deviation of the Hamming distance calculated between the colonies (42 ferromagnetic colonies with reporter vector 1; 65 ferromagnetic colonies with reporter vector 2) and 10 simulated populations for each value of T. The value of the Hamming distance was divided by the total number of pixels. Dotted vertical lines mark the critical value of T, and red solid lines mark the smallest average value of the Hamming distance. To compare the smallest average value of the Hamming distance with each other value, statistical analysis was performed using an ordinary One-Way ANOVA, followed by Dunnett's multiple comparisons test. ns (not significant): $P > 0.05$, $*$: $P \leq 0.05$, $**$: $P \leq 0.01$, $****$: $P \leq 0.0001$.

bioRxiv preprint doi: https://doi.org/10.1101/2023.05.10.540292; this version posted May 11, 2023. The copyright holder for this preprint (which was not certified by peer review) is the author/funder, who has granted bioRxiv a license to display the preprint in perpetuity. It is made available under aCC-BY-NC-ND 4.0 International license.

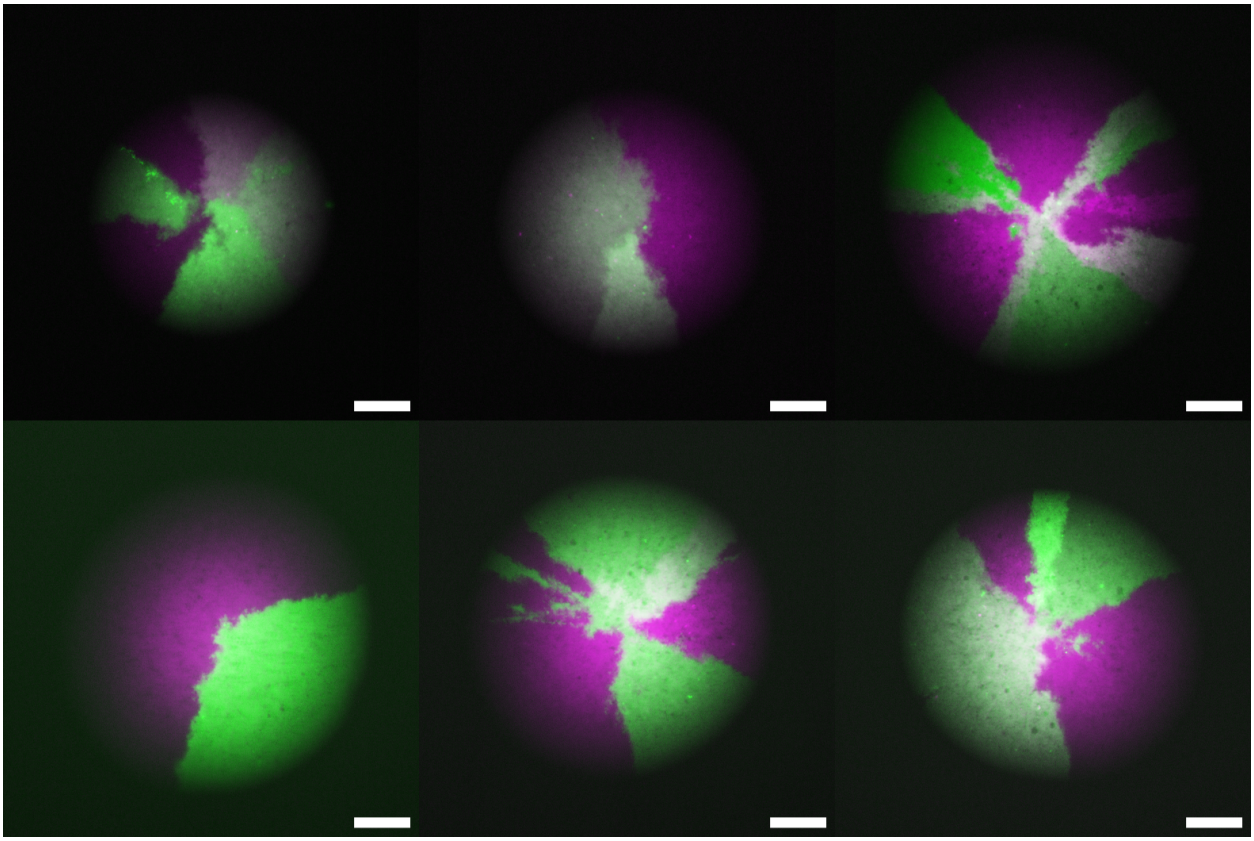

Figure S8: **Sharp boundaries generated between cellular state domains in colonies of spherical cells due to the segregation of fixed-state reporter vectors.** Representative images of the fluorescent patterns that emerge in colonies of spherical *E. coli* cells due to the segregation of fixed-state reporter vectors Nunez *et al* (2017). Each cell that gives rise to a colony that contains two plasmids: one encoding a red fluorescent protein, and another encoding a green fluorescent protein. The patterns generated in these colonies are the result of the segregation of these plasmids during cell division: once a cell loses one of these plasmids, its cellular state and the cellular state of all its progeny is fixed, generating sharp boundaries between the cellular state domains. Scale bars 100 μm. The backbone plasmids used in this assay were obtained from Nunez *et al* (2017).

bioRxiv preprint doi: https://doi.org/10.1101/2023.05.10.540292; this version posted May 11, 2023. The copyright holder for this preprint (which was not certified by peer review) is the author/funder, who has granted bioRxiv a license to display the preprint in perpetuity. It is made available under aCC-BY-NC-ND 4.0 International license.

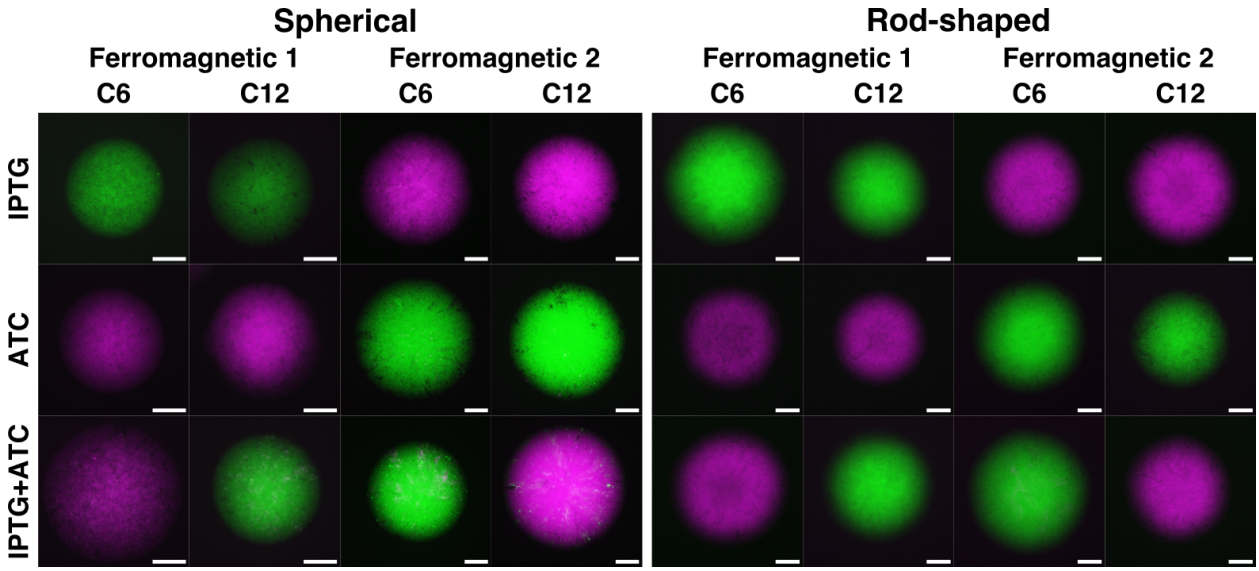

Figure S9: **Cellular state switch in ferromagnetic colonies grown on solid media supplemented with inhibitors.** Representative images of colonies of rod-shaped and spherical ferromagnetic cells that carry the reporter vector 1 (Ferromagnetic 1) or the reporter vector 2 (Ferromagnetic 2). Cells were grown on M9-glucose solid media supplemented C6HSL or C12HSL and with IPTG, ATC, or both inhibitors. These inhibitors bind to the repressors LacI and TetR, preventing them from repressing the expression of target genes. Thus, depending on the inhibitor present in the media, one state cannot be repressed, resulting in the repression of the other state, regardless of the coupling signal in which they are grown. Blocking both repressors at the same time, allows cells to adopt the cellular state induced by the coupling molecule present in the medium. Scale bars 100 μm.

bioRxiv preprint doi: https://doi.org/10.1101/2023.05.10.540292; this version posted May 11, 2023. The copyright holder for this preprint (which was not certified by peer review) is the author/funder, who has granted bioRxiv a license to display the preprint in perpetuity. It is made available under aCC-BY-NC-ND 4.0 International license.

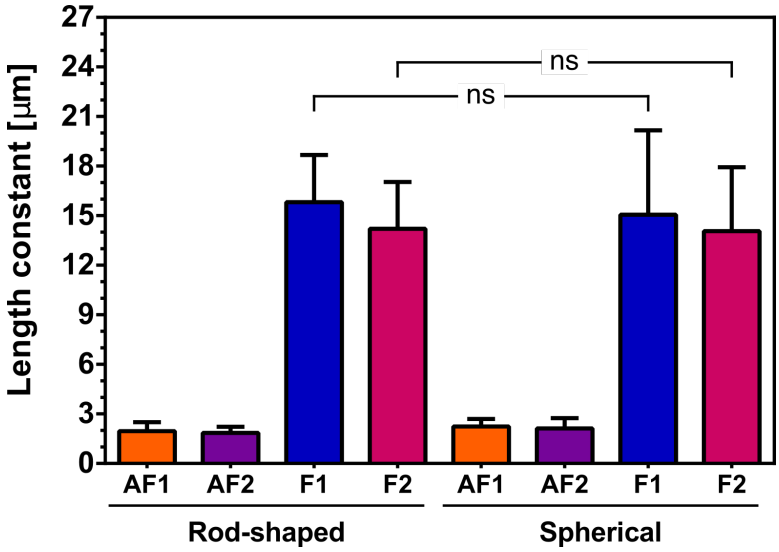

Figure S10: **Characteristic size of cellular states domains of ferromagnetic and anti-ferromagnetic colonies.** Length constants of ferromagnetic and anti-ferromagnetic colonies generated from rod-shaped and spherical cells, highlighting that there is no significant differences (P value: 0.0557 for F1 rod vs F1 sph and 0.4303 for F2 rod vs F2 sph) between the values of the length constants of ferromagnetic colonies of rod-shaped and spherical cells. Values correspond to the mean ± the standard deviation of the length constants obtained by fitting the exponential decay equation $y = y_0 * \exp(-x/b) + C$ to the data of sACF analysis, where the value of b corresponds to the length constant. Statistical analysis was performed using two-tailed Mann-Whitney test ($\alpha = 2.5\%$). ns (not significant): $P > 0.05$.

bioRxiv preprint doi: https://doi.org/10.1101/2023.05.10.540292; this version posted May 11, 2023. The copyright holder for this preprint (which was not certified by peer review) is the author/funder, who has granted bioRxiv a license to display the preprint in perpetuity. It is made available under aCC-BY-NC-ND 4.0 International license.

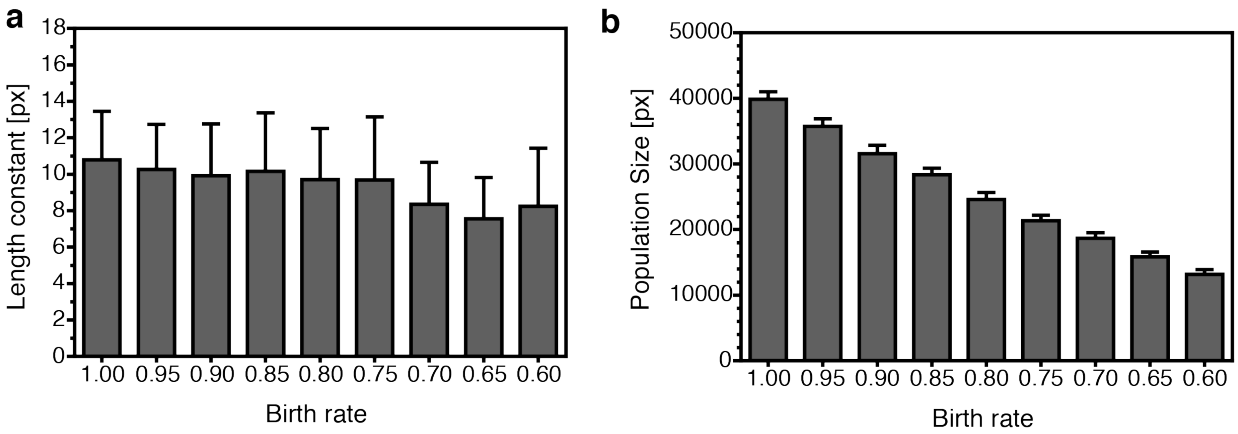

Figure S11: **Characteristic size of cellular state domains and average colony size of simulated populations with ferromagnetic interactions.** Length constant (a) and population size (b) of ferromagnetic colonies simulated with CPIM. While the size of the simulated population decreases as the value of the birth rate decreases, the mean size of the cellular states domains remains constant until the birth rate reaches a value of 0.75 (P value: 0.3049 for 1.00 vs 0.95, 0.0650 for 1.00 vs 0.90, 0.2037 for 1.00 vs 0.85, 0.0391 for 1.00 vs 0.80, 0.0117 for 1.00 vs 0.75, < 0.0001 for 1.00 vs 0.70, < 0.0001 for 1.00 vs 0.65, < 0.0001 for 1.00 vs 0.60). Statistical analysis was performed using unpaired two-tailed Mann-Whitney ($\alpha = 2.5\%$) comparing each column with the column corresponding to birth rate = 1.00

bioRxiv preprint doi: https://doi.org/10.1101/2023.05.10.540292; this version posted May 11, 2023. The copyright holder for this preprint (which was not certified by peer review) is the author/funder, who has granted bioRxiv a license to display the preprint in perpetuity. It is made available under aCC-BY-NC-ND 4.0 International license.

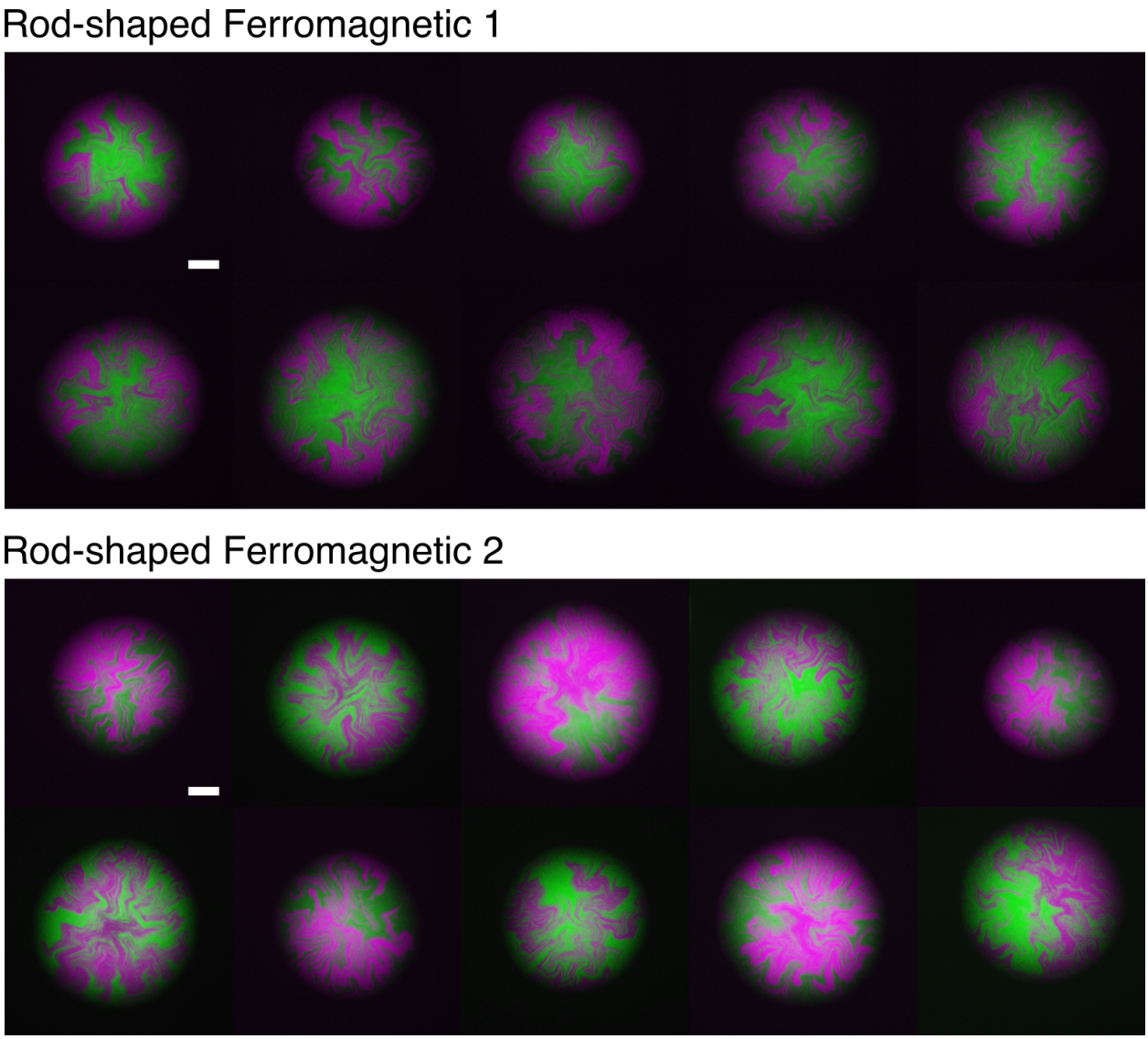

Figure S12: **Colonies of rod-shaped *E. coli* cells carrying the ferromagnetic system with reporter vector 1 or 2.** Scale bars 100 μm.

bioRxiv preprint doi: https://doi.org/10.1101/2023.05.10.540292; this version posted May 11, 2023. The copyright holder for this preprint (which was not certified by peer review) is the author/funder, who has granted bioRxiv a license to display the preprint in perpetuity. It is made available under aCC-BY-NC-ND 4.0 International license.

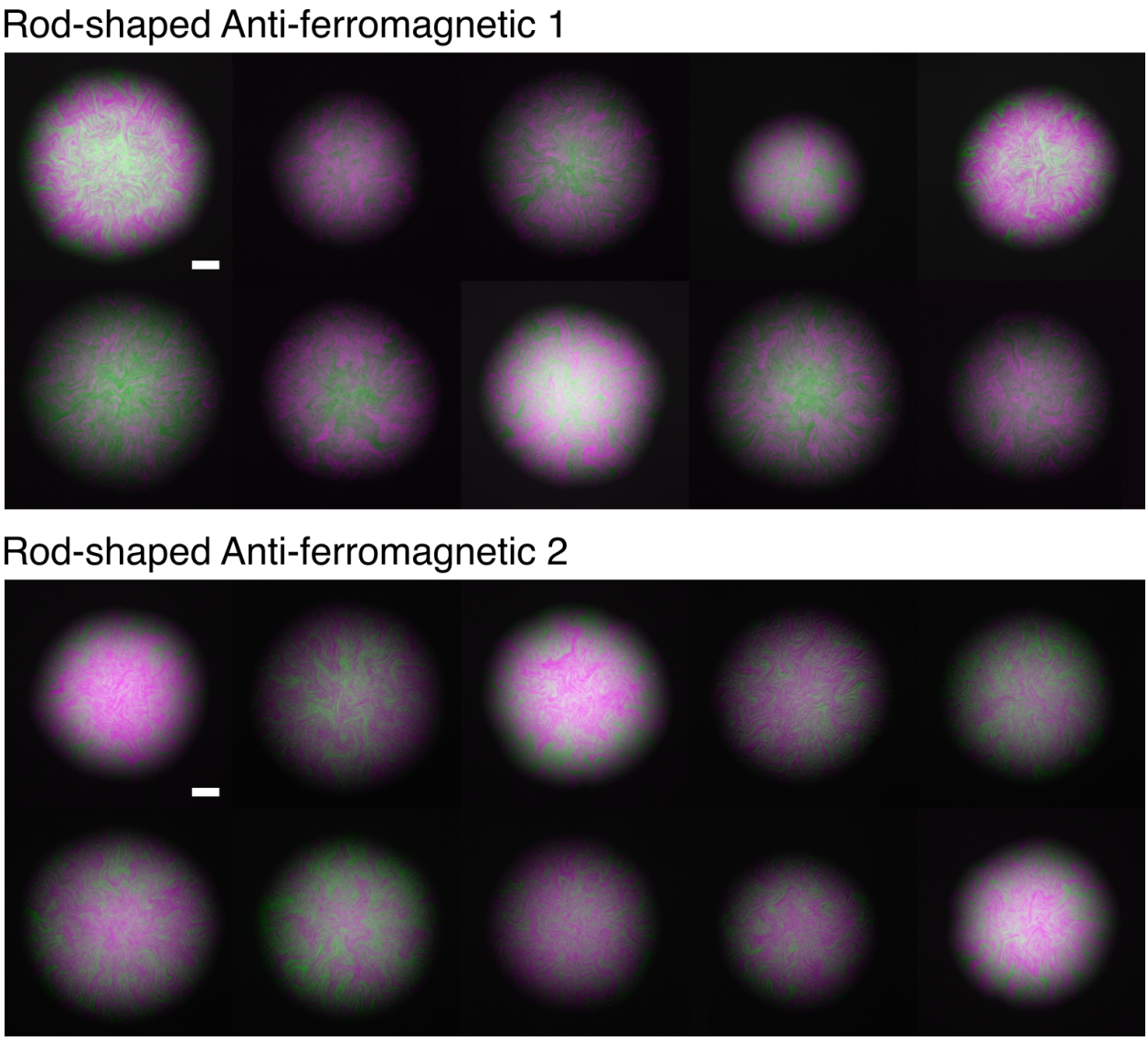

Figure S13: **Colonies of rod-shaped *E. coli* cells carrying the anti-ferromagnetic system with reporter vector 1 or 2.** Scale bars 100 μm.

bioRxiv preprint doi: https://doi.org/10.1101/2023.05.10.540292; this version posted May 11, 2023. The copyright holder for this preprint (which was not certified by peer review) is the author/funder, who has granted bioRxiv a license to display the preprint in perpetuity. It is made available under aCC-BY-NC-ND 4.0 International license.

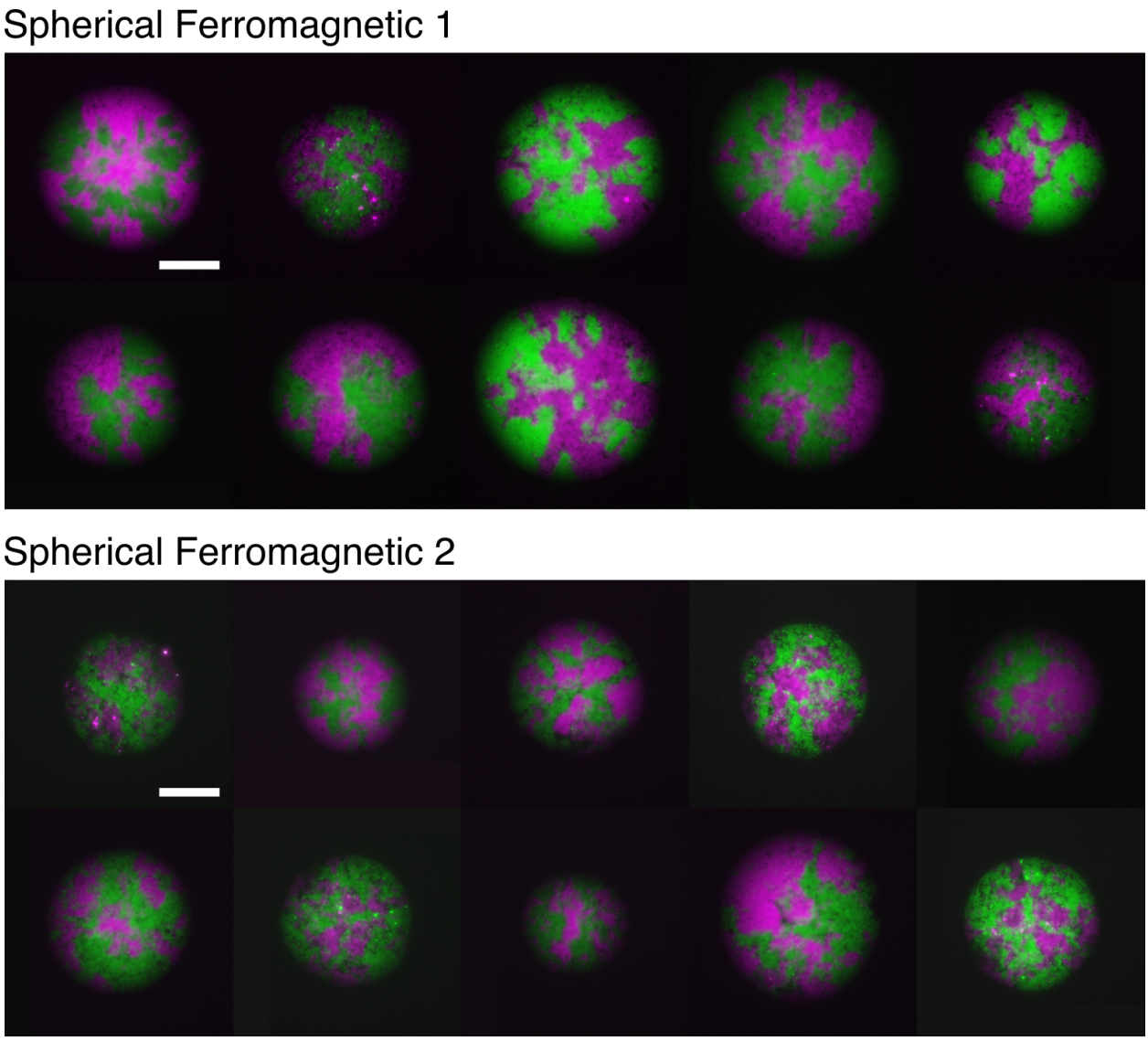

Figure S14: **Colonies of spherical *E. coli* cells carrying the ferromagnetic system with reporter vector 1 or 2.** Scale bars 100 μm.

bioRxiv preprint doi: https://doi.org/10.1101/2023.05.10.540292; this version posted May 11, 2023. The copyright holder for this preprint (which was not certified by peer review) is the author/funder, who has granted bioRxiv a license to display the preprint in perpetuity. It is made available under aCC-BY-NC-ND 4.0 International license.

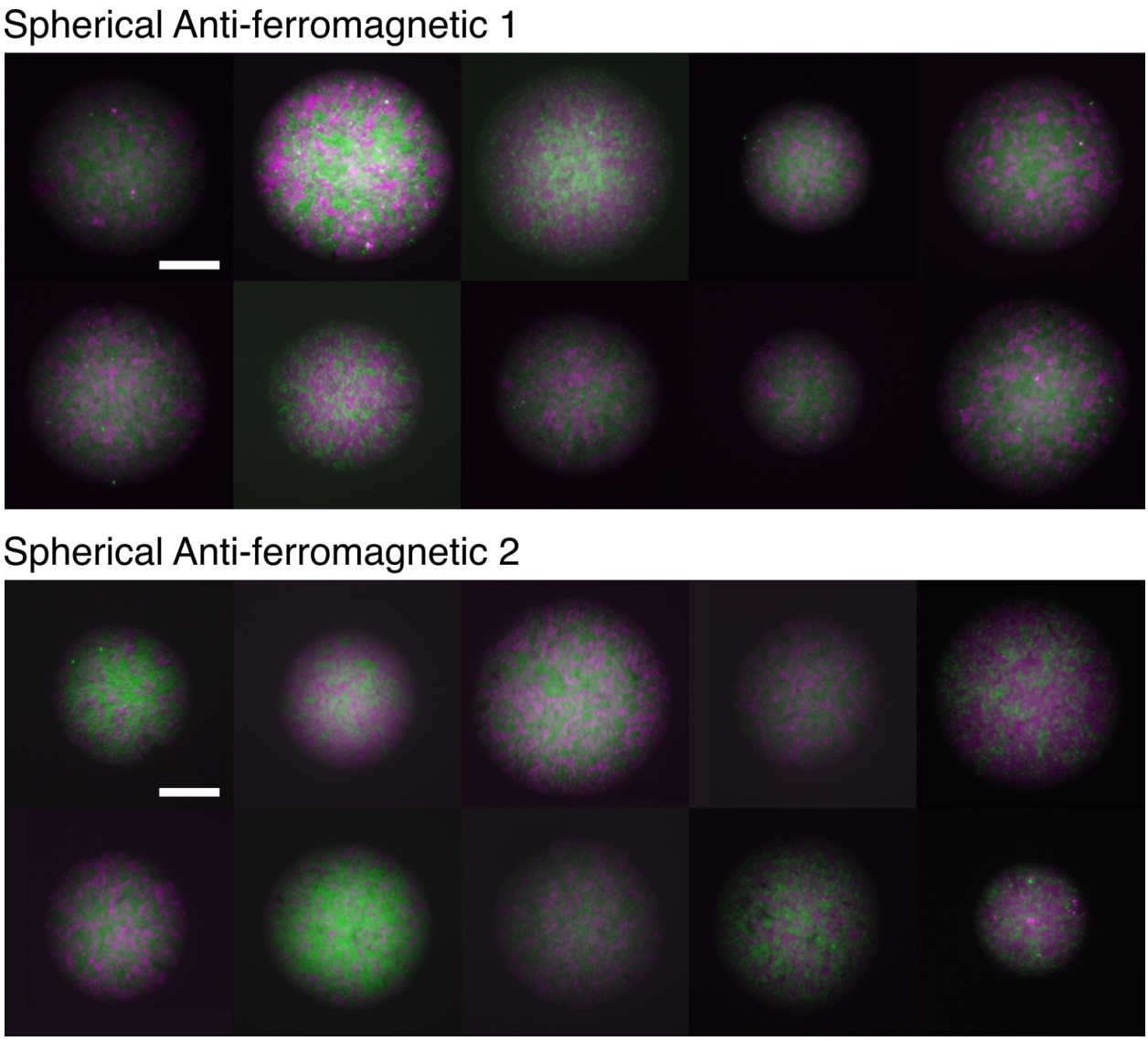

Figure S15: **Colonies of spherical *E. coli* cells carrying the anti-ferromagnetic system with reporter vector 1 or 2.** Scale bars 100 μm.

bioRxiv preprint doi: https://doi.org/10.1101/2023.05.10.540292; this version posted May 11, 2023. The copyright holder for this preprint (which was not certified by peer review) is the author/funder, who has granted bioRxiv a license to display the preprint in perpetuity. It is made available under aCC-BY-NC-ND 4.0 International license.

Table S1: Plasmids used in this study

Name	**Resistance**	**Ori**	**Relevant features**	**Reference**
AFM_1XpSC101	Kanamycin	pSC101	Antiferromagnetic vector	This work `https://benchling.com/s/seq-HRNLsPKCw1V6ku5AuSqU?m=slm-mpV6arDE3Vf6zZsH13WZ`
AFM_1XpSC101_spect	Spectinomycin	pSC101	Antiferromagnetic vector	This work `https://benchling.com/s/seq-FJ96M0uVIOSAmUbApEng?m=slm-unIXNAA7BUNLEkTZfqkC`
FM_1XpSC101	Kanamycin	pSC101	Ferromagnetic vector	This work `https://benchling.com/s/seq-f8I0wyDhZNWanhSYtHhn?m=slm-j1uwY4Ch66965MWCVCPY`
FM_1XpSC101_spect	Spectinomycin	pSC101	Ferromagnetic vector	This work `https://benchling.com/s/seq-u3pgZVu0haXHsnppnbrc?m=slm-LkgbXuMaGWG5YvhEJox5`
R1_A0_col2	Chloramphenicol and Carbenicillin	pDestBAC	Reporter vector 1	This work `https://benchling.com/s/seq-KRt1wTzO77TiISQS53hu?m=slm-FP8KxGkrVimOqB3KLed3`
R2_A0_col2	Chloramphenicol and Carbenicillin	pDestBAC	Reporter vector 2	This work `https://benchling.com/s/seq-bp0havwRwbXDq7FQ7RGc?m=slm-JXGGK11HJlsW7nQagxy3`
SEG10	Chloramphenicol and Carbenicillin	pDestBAC	SEG vector expressing sfGFP	Nunez *et al* (2017)
SEG11	Chloramphenicol and Tetracycline	pDestBAC	SEG vector expressing mCherry	Nunez *et al* (2017)

bioRxiv preprint doi: https://doi.org/10.1101/2023.05.10.540292; this version posted May 11, 2023. The copyright holder for this preprint (which was not certified by peer review) is the author/funder, who has granted bioRxiv a license to display the preprint in perpetuity. It is made available under aCC-BY-NC-ND 4.0 International license.

Table S2: Reporter

	C6HSL		C12HSL	
	RFP promoter	*GFP* promoter	*RFP* promoter	*GFP* promoter
n	1.00	1.00	1.00	1.00
ΔE [k_BT]	-3.40	-4.20	-3.80	-4.00
Kdoff [M]	1.60E-05	2.20E-07	1.80E-07	1.00E-04
Kdon [M]	4.30E-10	1.70E-08	6.20E-08	2.00E-09

Table S3: Ferromagnetic

	C6HSL		C12HSL	
	RFP promoter	*GFP* promoter	*RFP* promoter	*GFP* promoter
n	1.45	2.50	1.00	1.00
ΔE [k_BT]	-6.60	6.20	-6.60	5.60
Kdoff [M]	1.00E-06	1.00E-11	4.50E-04	1.60E-09
Kdon [M]	1.90E-11	2.70E-08	1.20E-08	2.10E-07

Table S4: Anti-Ferromagnetic

	C6HSL		C12HSL	
	RFP promoter	*GFP* promoter	*RFP* promoter	*GFP* promoter
n	1.00	1.00	1.00	1.00
ΔE [k_BT]	-1.20	-0.40	-1.20	-0.30
Kdoff [M]	9.00E-04	1.60E-08	1.80E-09	1.00E-05
Kdon [M]	1.80E-08	1.40E-07	2.60E-08	1.80E-09

Biological parameters that characterize the binding of the inducers C6HSL and C12HSL to the *RFP* and *GFP* promoters in cells carrying the reporter vector (Table S2), the ferromagnetic system (Table S3) or the anti-ferromagnetic system (Table S4). The values were obtained from the fit to Eq. 2 of the data of red and green fluorescent protein synthesis rates of liquid cultures of cells carrying these systems as a function of the inducer concentrations.

bioRxiv preprint doi: https://doi.org/10.1101/2023.05.10.540292; this version posted May 11, 2023. The copyright holder for this preprint (which was not certified by peer review) is the author/funder, who has granted bioRxiv a license to display the preprint in perpetuity. It is made available under aCC-BY-NC-ND 4.0 International license.

Table S5: **Scaling exponent γ of populations with ferromagnetic interactions.**

	Scaling exponent γ	
	r_plfit	Least squares fit (inset)
CPIM	1.9271	1.958
Rod-shaped Ferro R.V.1	2.1739	2.175
Rod-shaped Ferro R.V.2	2.1369	2.086
Spherical Ferro R.V.1	1.9095	2.126
Spherical Ferro R.V.2	1.7593	1.866
Spherical Ferro GLY	2.3073	2.227
Spherical Ferro GLU	2.1918	2.141

Power-law exponents of ferromagnetic populations simulated with CPIM at $T = T_c$, ferromagnetic colonies of rod-shaped and spherical cells (Fig. 4d), and ferromagnetic colonies of spherical cells grown in minimal medium supplemented with glucose (GLU) or glycine (GLY) (Fig. 4e). The exponents were estimated using the r_plfit(k,'hist') algorithm Hanel *et al* (2017) or by the the least squares method.

Table S6: **Scaling exponent γ of simulated populations with ferromagnetic interactions at different birth rates.**

	Scaling exponent γ	
Birth rate	r_plfit	Least squares fit
1.00	1.921	1.946
0.95	1.911	1.921
0.90	1.926	1.987
0.85	1.916	1.962
0.80	1.922	1.958
0.75	1.900	1.923

Power-law exponents of ferromagnetic population of Fig. 4e simulated with CPIM at different cell birth rates. The exponents were estimated using the r_plfit(k,'hist') algorithm (Hanel *et al* (2017)) or by the least squares method.

References

Basu S, Gerchman Y, Collins CH, Arnold FH, Weiss R (2005) A synthetic multicellular system for programmed pattern formation. *Nature* **434**: 1130–1134

Begg KJ, Donachie WD (1998) Division planes alternate in spherical cells of *Escherichia coli*. *J Bacteriol* **180**: 2564–7

Bittihn P, Din MO, Tsimring LS, Hasty J (2018) Rational engineering of synthetic microbial systems: from single cells to consortia. *Curr Opin Microbiol* **45**: 92–99

Blanchard AE, Lu T (2015) Bacterial social interactions drive the emergence of differential spatial colony structures. *BMC Syst Biol* **9**: 59

Bray D, Duke T (2004) Conformational spread: the propagation of allosteric states in large multiprotein complexes. *Annu Rev Biophys Biomol Struct* **33**: 53–73

Cole JA, Kohler L, Hedhli J, Luthey-Schulten Z (2015) Spatially-resolved metabolic cooperativity within dense bacterial colonies. *BMC Syst Biol* **9**: 15

bioRxiv preprint doi: https://doi.org/10.1101/2023.05.10.540292; this version posted May 11, 2023. The copyright holder for this preprint (which was not certified by peer review) is the author/funder, who has granted bioRxiv a license to display the preprint in perpetuity. It is made available under aCC-BY-NC-ND 4.0 International license.

Collier JR, Monk NAM, Maini PK, Lewis JH (1996) Pattern Formation by Lateral Inhibition with Feedback: a Mathematical Model of Delta-Notch Intercellular Signalling. *Journal of Theoretical Biology* **183**: 429–446

Dal Co A, van Vliet S, Ackermann M (2019) Emergent microscale gradients give rise to metabolic cross-feeding and antibiotic tolerance in clonal bacterial populations. *Philosophical Transactions of the Royal Society B Biological Sciences* **374**: 20190080

Dal Co A, van Vliet S, Kiviet DJ, Schlegel S, Ackermann M (2020) Short-range interactions govern the dynamics and functions of microbial communities. *Nature Ecology Evolution* **4**: 366–375

Davies J (2017) Using synthetic biology to explore principles of development. *Development* **144**: 1146–1158

Davies JA, Glykofrydis F (2020) Engineering pattern formation and morphogenesis. *Biochemical Society Transactions* **48**: 1177–1185

Duke TA, Le Novere N, Bray D (2001) Conformational spread in a ring of proteins: a stochastic approach to allostery. *J Mol Biol* **308**: 541–53

Ebrahimkhani MR, Ebisuya M (2019) Synthetic developmental biology: build and control multicellular systems. *Curr Opin Chem Biol* **52**: 9–15

Ebrahimkhani MR, Levin M (2021) Synthetic living machines: A new window on life. *iScience* **24**: 102505

Elowitz M, Lim WA (2010) Build life to understand it. *Nature* **468**: 889–90

Elowitz MB, Leibler S (2000) A synthetic oscillatory network of transcriptional regulators. *Nature* **403**: 335–8

Engler C, Kandzia R, Marillonnet S (2008) A one pot, one step, precision cloning method with high throughput capability. *PLoS One* **3**: e3647

Gardner TS, Cantor CR, Collins JJ (2000) Construction of a genetic toggle switch in *Escherichia coli*. *Nature* **403**: 339–42

Gibson DG, Young L, Chuang RY, Venter JC, Hutchison C. A. r, Smith HO (2009) Enzymatic assembly of DNA molecules up to several hundred kilobases. *Nat Methods* **6**: 343–5

Goldenfeld N (1992) *Lectures On Phase Transitions And The Renormalization Group*. Frontiers in physics. Boca Raton: Westview Press

Grant PK, Dalchau N, Brown JR, Federici F, Rudge TJ, Yordanov B, Patange O, Phillips A, Haseloff J (2016) Orthogonal intercellular signaling for programmed spatial behavior. *Mol Syst Biol* **12**: 849

Hanel R, Corominas-Murtra B, Liu B, Thurner S (2017) Fitting power-laws in empirical data with estimators that work for all exponents. *PLoS One* **12**: e0170920

Harris TE (1974) Contact Interactions on a Lattice. *Ann Probab* **2**: 969–988

Ibarra-García-Padilla E, Malanche-Flores CG, Poveda-Cuevas FJ (2016) The hobbyhorse of magnetic systems: the Ising model. *European Journal of Physics* **37**: 065103

Ising E (1925) Beitrag zur Theorie des Ferromagnetismus. *Zeitschrift fur Physik* **31**: 253–258

Iverson SV, Haddock TL, Beal J, Densmore DM (2016) CIDAR MoClo: Improved MoClo Assembly Standard and New *E. coli* Part Library Enable Rapid Combinatorial Design for Synthetic and Traditional Biology. *ACS Synth Biol* **5**: 99–103

Johnson MB, March AR, Morsut L (2017) Engineering multicellular systems: Using synthetic biology to control tissue self-organization. *Current Opinion in Biomedical Engineering* **4**: 163–173

bioRxiv preprint doi: https://doi.org/10.1101/2023.05.10.540292; this version posted May 11, 2023. The copyright holder for this preprint (which was not certified by peer review) is the author/funder, who has granted bioRxiv a license to display the preprint in perpetuity. It is made available under aCC-BY-NC-ND 4.0 International license.

Keymer JE, Endres RG, Skoge M, Meir Y, Wingreen NS (2006) Chemosensing in *Escherichia coli*: Two regimes of two-state receptors. *Proceedings of the National Academy of Sciences of the United States of America* **103**: 1786–1791

Kim JK, Chen Y, Hirning AJ, Alnahhas RN, Josić K, Bennett MR (2019) Long-range temporal coordination of gene expression in synthetic microbial consortia. *Nature Chemical Biology* **15**: 1102–1109

Kobe S (1997) Ernst Ising—Physicist and Teacher. *Journal of Statistical Physics* **88**: 991–995

Kylilis N, Tuza ZA, Stan GB, Polizzi KM (2018) Tools for engineering coordinated system behaviour in synthetic microbial consortia. *Nat Commun* **9**: 2677

Landau DP, Binder K (2014) *A Guide to Monte Carlo Simulations in Statistical Physics*. Cambridge: Cambridge University Press, 4 edition

Larkin JW, Zhai X, Kikuchi K, Redford SE, Prindle A, Liu J, Greenfield S, Walczak AM, Garcia-Ojalvo J, Mugler A, Süel GM (2018) Signal Percolation within a Bacterial Community. *Cell Syst* **7**: 137–145.e3

Liu J, Martinez-Corral R, Prindle A, Lee DD, Larkin J, Gabalda-Sagarra M, Garcia-Ojalvo J, Suel GM (2017) Coupling between distant biofilms and emergence of nutrient time-sharing. *Science* **356**: 638–642

Liu J, Prindle A, Humphries J, Gabalda-Sagarra M, Asally M, Lee DY, Ly S, Garcia-Ojalvo J, Suel GM (2015) Metabolic co-dependence gives rise to collective oscillations within biofilms. *Nature* **523**: 550–4

Lovley DR (2017) Happy together: microbial communities that hook up to swap electrons. *The ISME Journal* **11**: 327–336

Luo N, Wang S, You L (2019) Synthetic Pattern Formation. *Biochemistry* **58**: 1478–1483

Mee MT, Collins JJ, Church GM, Wang HH (2014) Syntrophic exchange in synthetic microbial communities. *Proc Natl Acad Sci U S A* **111**: E2149–56

Metropolis N, Rosenbluth AW, Rosenbluth MN, Teller AH, Teller E (1953) Equation of State Calculations by Fast Computing Machines. *The Journal of Chemical Physics* **21**: 1087–1092

Mukherji S, van Oudenaarden A (2009) Synthetic biology: understanding biological design from synthetic circuits. *Nature Reviews Genetics* **10**: 859 EP –

Nguyen PQ, Courchesne NMD, Duraj-Thatte A, Praveschotinunt P, Joshi NS (2018) Engineered Living Materials: Prospects and Challenges for Using Biological Systems to Direct the Assembly of Smart Materials. *Advanced materials Deerfield Beach Fla* **30**: e1704847–e1704847

Nielsen AAK, Der BS, Shin J, Vaidyanathan P, Paralanov V, Strychalski EA, Ross D, Densmore D, Voigt CA (2016) Genetic circuit design automation. *Science* **352**: aac7341

Noble AE, Machta J, Hastings A (2015) Emergent long-range synchronization of oscillating ecological populations without external forcing described by Ising universality. *Nat Commun* **6**: 6664

Noble AE, Rosenstock TS, Brown PH, Machta J, Hastings A (2018) Spatial patterns of tree yield explained by endogenous forces through a correspondence between the Ising model and ecology. *Proc Natl Acad Sci U S A* **115**: 1825–1830

Nounou MN, Bakshi BR (2000) Multiscale Methods for Denoising and Compression, In *Wavelets in Chemistry*, volume 22 of *Data Handling in Science and Technology*, : Elsevier, pp. 119 – 150

Nunez IN, Matute TF, Del Valle ID, Kan A, Choksi A, Endy D, Haseloff J, Rudge TJ, Federici F (2017) Artificial Symmetry-Breaking for Morphogenetic Engineering Bacterial Colonies. *ACS Synth Biol* **6**: 256–265

Payne S, Li B, Cao Y, Schaeffer D, Ryser MD, You L (2013) Temporal control of self-organized pattern formation without morphogen gradients in bacteria. *Molecular Systems Biology* **9**: 697

bioRxiv preprint doi: https://doi.org/10.1101/2023.05.10.540292; this version posted May 11, 2023. The copyright holder for this preprint (which was not certified by peer review) is the author/funder, who has granted bioRxiv a license to display the preprint in perpetuity. It is made available under aCC-BY-NC-ND 4.0 International license.

Rosenthal AZ, Qi Y, Hormoz S, Park J, Li SH, Elowitz MB (2018) Metabolic interactions between dynamic bacterial subpopulations. *Elife* **7**

Rudge TJ, Brown JR, Federici F, Dalchau N, Phillips A, Ajioka JW, Haseloff J (2016) Characterization of Intrinsic Properties of Promoters. *ACS Synth Biol* **5**: 89–98

Rudge TJ, Federici F, Steiner PJ, Kan A, Haseloff J (2013) Cell polarity-driven instability generates self-organized, fractal patterning of cell layers. *ACS Synth Biol* **2**: 705–14

Santos-Moreno J, Schaerli Y (2019) Using Synthetic Biology to Engineer Spatial Patterns. *Advanced Biosystems* **3**: 1800280

Schaerli Y, Munteanu A, Gili M, Cotterell J, Sharpe J, Isalan M (2014) A unified design space of synthetic stripe-forming networks. *Nature Communications* **5**: 4905

Schindelin J, Arganda-Carreras I, Frise E, Kaynig V, Longair M, Pietzsch T, Preibisch S, Rueden C, Saalfeld S, Schmid B, Tinevez JY, White DJ, Hartenstein V, Eliceiri K, Tomancak P, Cardona A (2012) Fiji: an open-source platform for biological-image analysis. *Nat Methods* **9**: 676–82

Shapiro JA (1998) Thinking about bacterial populations as multicellular organisms. *Annu Rev Microbiol* **52**: 81–104

Shen Y, Chen Y, Wu J, Shaner NC, Campbell RE (2017) Engineering of mCherry variants with long Stokes shift, red-shifted fluorescence, and low cytotoxicity. *PloS one* **12**: e0171257–e0171257

Solé R, Ollé-Vila A, Vidiella B, Duran-Nebreda S, Conde-Pueyo N (2018) The road to synthetic multicellularity. *Current Opinion in Systems Biology* **7**: 60–67

Solé RV (2011) *Phase Transitions*. : Princeton University Press

Stauffer D, Aharony A (1994) *Introduction to percolation theory*. London ; Bristol, PA: Taylor & Francis, rev., 2nd edition, 94200274 Dietrich Stauffer and Amnon Aharony. ill. ; 24 cm. Includes bibliographical references and index.

Taheri-Araghi S, Bradde S, Sauls J, Hill N, Levin P, Paulsson J, Vergassola M, Jun S (2015) Cell-Size Control and Homeostasis in Bacteria. *Current Biology* **25**: 385–391

Teague BP, Guye P, Weiss R (2016) Synthetic Morphogenesis. *Cold Spring Harb Perspect Biol* **8**

Toda S, Blauch LR, Tang SKY, Morsut L, Lim WA (2018) Programming self-organizing multicellular structures with synthetic cell-cell signaling. *Science* **361**: 156–162

Turing AM (1990) The chemical basis of morphogenesis. 1953. *Bull Math Biol* **52**: 153–97; discussion 119–52

van Gestel J, Bareia T, Tenennbaum B, Dal Co A, Guler P, Aframian N, Puyesky S, Grinberg I, D'Souza GG, Erez Z, Ackermann M, Eldar A (2021) Short-range quorum sensing controls horizontal gene transfer at micron scale in bacterial communities. *Nature Communications* **12**: 2324

van Vliet S, Dal Co A, Winkler AR, Spriewald S, Stecher B, Ackermann M (2018) Spatially Correlated Gene Expression in Bacterial Groups: The Role of Lineage History, Spatial Gradients, and Cell-Cell Interactions. *Cell Systems* **6**: 496–507.e6

van Vliet S, Hauert C, Fridberg K, Ackermann M, Dal Co A (2022) Global dynamics of microbial communities emerge from local interaction rules. *PLOS Computational Biology* **18**: 1–23

Walter V (2017) *Lipid membrane interaction with self-assembling cell-penetrating peptides*. Phd thesis, Université de Strasbourg

Wang Y, Badea T, Nathans J (2006) Order from disorder: Self-organization in mammalian hair patterning. *Proceedings of the National Academy of Sciences* **103**: 19800–19805

bioRxiv preprint doi: https://doi.org/10.1101/2023.05.10.540292; this version posted May 11, 2023. The copyright holder for this preprint (which was not certified by peer review) is the author/funder, who has granted bioRxiv a license to display the preprint in perpetuity. It is made available under aCC-BY-NC-ND 4.0 International license.

Weber M, Buceta J (2016) The cellular Ising model: a framework for phase transitions in multicellular environments. *J R Soc Interface* **13**

Wioland H, Woodhouse FG, Dunkel J, Goldstein RE (2016) Ferromagnetic and antiferromagnetic order in bacterial vortex lattices. *Nat Phys* **12**: 341–345